GERMAN-MONGOLIAN INSTITUTE FOR RESOURCES AND TECHNOLOGY

Faculty of Mechanical and Electrical Engineering

Master's Thesis

Inference of Subsidence Prediction Model Parameters Based on InSAR Data

By: Suvd-Erdene Tsend-Ayush

Student ID: M2320002

First supervisor:	Prof. Dr. Jörg Benndorf, TU Bergakademie Freiberg
Second supervisor:	Prof. Altangerel Lkhamsuren, GMIT Nalaikh

Ulaanbaatar, Mongolia

12/5/2025

GERMAN-MONGOLIAN INSTITUTE FOR RESOURCES AND TECHNOLOGY

Statutory Declaration

Tsend-Ayush, Suvd-Erdene	M2320002
Last Name, First Name	Student ID Number

I hereby declare that I have prepared the submitted master's thesis

"Inference of Subsidence Prediction Model Parameters Based on InSAR Data"

independently and without unauthorized external assistance. I have not used any sources or aids other than those listed in the bibliography.

If the work is additionally submitted in electronic form, I confirm that the written and electronic versions are identical.

This thesis has not been submitted, either in full or in part, to any other examination authority in the same or a similar form.

Ulaanbaatar, Mongolia 3 Dec, 2025	
Place, Date	Signature

Acknowledgement

I would like to express my sincere gratitude to Prof. Dr. Jörg Benndorf for supervising my thesis during my semester abroad at TU Bergakademie Freiberg. Although the exchange semester was mainly intended for coursework, he supported my request to complete my thesis under his supervision and provided helpful guidance throughout the modules I took from his teaching program. His advice and feedback played an important role in shaping this work.

I also thank Prof. Altangerel Lkhamsuren for his supervision, comments and continued support throughout my studies at GMIT. I am grateful to both professors for their valuable time, thoughtful discussions and constructive suggestions.

I would also like to thank the German-Mongolian Institute for Resources and Technology (GMIT) for supporting my participation in the DAAD-funded semester exchange and for their coordination throughout the process.

I am grateful to the faculty and staff of both institutions for their assistance during my studies, and to my colleagues and friends for their discussions and support during the development of this thesis.

Finally, I thank my family for their constant encouragement and understanding, which made it possible for me to complete this thesis alongside my academic and personal responsibilities.

Abstract

Mining and storage operations can cause ground subsidence that threatens infrastructure. Satellite InSAR measures millimeter-level motion but only along the radar line of sight, which mixes vertical and horizontal components. This thesis builds a controlled synthetic framework to test how well three subsidence parameters - the influence angle β, convergence rate μ, and horizontal-tilt factor λ can be recovered from synthetic InSAR line-of-sight (LOS) data. A Gaussian influence function generates vertical, tilt, and horizontal fields that are projected into ascending and descending viewing geometries and perturbed with 1–2 mm Gaussian noise. A series of numerical experiments were performed, including baseline inversion, ASC-only vs. DES-only geometry tests, noise-level sensitivity, and multi-scenario horizontal-factor cases (λ = 0.3, 0.5, 1.0).

Parameters are estimated with weighted nonlinear least squares and assessed with residual diagnostics, Monte-Carlo uncertainty, and sensitivity tests for noise and geometry. Limited Bayesian (MCMC) and Extended Kalman Filter (EKF) trials demonstrate probabilistic and sequential extensions.

Results show accurate recovery of (β, μ, λ) with residuals at the noise level (~1 mm). Histograms and Q–Q plots indicate near-normal errors, and per-orbit RMSE closely matches the standard deviation. Using both orbits (ASC+DES) reduces uncertainty relative to single-track inversions and weakens parameter coupling, especially for λ. Monte-Carlo spreads are narrow and scale with noise as expected. The Bayesian and EKF tests agree with the deterministic solution and provide credible intervals and time-update capability. These findings support combined-geometry InSAR as a practical basis for estimating subsidence parameters and suggest a clear path to applying the framework to real time-series.

GERMAN-MONGOLIAN INSTITUTE FOR RESOURCES AND TECHNOLOGY

Table of Contents

Table of Figures

Figures in Appendix

1 Introduction

Subsidence occurs in both natural and human settings and can threaten roads, pipelines, buildings, and utilities. Natural drivers include karst dissolution, sediment compaction, and tectonic deformation; common human drivers include groundwater withdrawal, underground mining, and tunneling (Galloway & Burbey, 2011). Traditional geodetic techniques such as leveling and GPS provide high accuracy, but their limited coverage and cost restrict broad application. Reliable prediction and monitoring are essential for risk mitigation and planning. In this context, Interferometric Synthetic Aperture Radar (InSAR) provides dense, wide-area measurements with millimeter-scale sensitivity and has become a core tool for deformation analysis (Bürgmann et al., 2000).

InSAR measures displacement precisely but senses only motion along the radar line of sight (LOS). A single LOS mixes vertical subsidence, horizontal displacement, and tilt, and cannot recover full 3-D motion on its own; sensitivity is strongest to vertical and east–west motion and weakest to north–south (Zebker & Villasenor, 1992; Samieie-Esfahany et al., 2009). Converting LOS to “vertical” by dividing by the cosine of the incidence angle ignores horizontal motion and can bias estimates where lateral components are significant (Hanssen, 2001; Yang et al., 2016; Wang et al., 2018). Reliable recovery of physically meaningful parameters therefore requires multiple imaging geometries and/or inversion with physical constraints (Fuhrmann & Garthwaite, 2019; Witkowski et al., 2021; Dong et al., 2021).

Motivated by these limitations, this thesis asks how reliably β, μ, and λ can be recovered from LOS data under realistic geometry and mm-level noise, using a controlled synthetic framework. A Gaussian influence-function generates vertical, tilt, and horizontal fields, which are projected into ascending (ASC) and descending (DES) LOS and perturbed with Gaussian noise. The aim and objectives that follow specify the estimation and evaluation steps.

Research Aim and Objectives

The aim is to build and test a synthetic yet realistic framework that links underground deformation to its line-of-sight (LOS) representation and quantifies how well β, μ, λ can be recovered from InSAR observations under known geometry and noise.

Objectives:

1. Forward model: implement a Python-based Gaussian influence-function that simulates vertical subsidence, surface tilt, and horizontal displacement.
2. LOS projection: map the 3-D fields into ascending and descending LOS using explicit incidence and azimuth angles.
3. Parameter estimation: invert for (β, μ, λ) with weighted nonlinear least squares; assess fit with residual maps, histograms, and Q–Q plots; quantify uncertainty and parameter coupling with Monte Carlo experiments and sensitivity tests (noise, geometry).
4. Cross-checks: use Bayesian MCMC to obtain posterior intervals and an Extended Kalman Filter to demonstrate sequential updates for multiple epochs.

Research Questions

This thesis is guided by the following research questions:

RQ1. How well can the three key subsidence parameters - the influence angle β, convergence rate μ, and horizontal-tilt factor λ - be recovered from synthetic InSAR line-of-sight (LOS) data under Sentinel-1-like viewing geometry and millimeter-level noise?

RQ2. How does the choice of satellite viewing geometry (ascending-only, descending-only, or combined ASC+DES) influence the uncertainty in β, μ, and λ and the way these parameters depend on one another?

RQ3. How sensitive are the estimated parameters to the level of LOS noise, and how do noise and geometry together affect the stability and reliability of the inversion?

RQ4. What additional value do Bayesian (MCMC) and sequential (Extended Kalman Filter) approaches provide, compared with the baseline weighted nonlinear least-squares solution, for quantifying uncertainty and updating the parameters over time?

Contributions of this Thesis

This thesis offers several contributions to understanding how reliably subsidence parameters can be inferred from InSAR LOS observations under controlled synthetic conditions. The key contributions are:

1. A reproducible evaluation framework: a clear forward–inverse structure is established to test the recoverability of β, μ, and λ under realistic Sentinel-1-like geometry and millimeter-level noise.
2. Quantitative assessment of parameter recovery: through least-squares inversion and Monte Carlo simulations, the study provides measurable evidence that these parameters can be recovered with high accuracy and stable uncertainty behavior.
3. Insight into the role of viewing geometry and noise: systematic tests show how ASC-only, DES-only, and combined ASC+DES datasets affect parameter uncertainty and coupling, highlighting the practical value of dual-geometry observations.
4. Demonstration of probabilistic and sequential extensions: Bayesian sampling and Extended Kalman Filtering are used to illustrate how the

same framework can support uncertainty quantification and multi-epoch updating.

The workflow is evaluated through several numerical experiments, including a baseline synthetic case, λ-scenario tests, ASC-only vs. DES-only geometry comparisons, and noise-sensitivity analysis. All experiments use synthetic data with an axisymmetric Gaussian kernel and independent, homoscedastic LOS noise (1–2 mm). Two viewing geometries (ASC and DES) are considered; full 3D decomposition is not attempted. The study focuses on parameter recoverability and uncertainty under controlled conditions; atmospheric correlation, unwrapping errors, and site heterogeneity are noted as future extensions.

Chapter 2 provides an overview of subsidence mechanisms, classical influence-function models, and InSAR-based parameter estimation. Chapter 3 presents the analytical subsidence model, LOS projection, synthetic data generation, and inversion framework. Chapter 4 reports the forward simulations, parameter-estimation results, and sensitivity analyses. Chapter 5 discusses the implications, strengths, and limitations of the approach. Chapter 6 concludes the thesis and outlines directions for future work.

2 State of the Art

2.1 Subsidence Overview

Subsidence describes the downward movement of the ground surface when the material supporting it at depth is removed or loses strength (Kratzsch, 1983; Whittaker & Reddish, 1989). The change may be gradual, taking place over months or years, or abrupt enough to cause immediate damage. It can affect areas of very different scales, from shallow depressions covering only a few meters to large regional sags extending for kilometers. Both natural and human processes can cause subsidence. In natural environments, it develops through the dissolution of rock in karst landscapes, the compaction of loose sediments, volcanic activity, or tectonic movement (Chaussard et al., 2013; Galloway & Burbey, 2011). Human activities, in contrast, are often more concentrated in space and time, with underground mining, groundwater withdrawal, tunneling, and hydrocarbon extraction being the main causes in industrialized regions (Bell et al., 2000); Herrera et al., 2021). It has been reported in many parts of the world for decades and can damage both underground and surface structures, posing safety risks for people. This makes it important to keep developing ways to reduce its environmental impact (Guzy & Witkowski, 2021).

In natural settings, the processes that lead to subsidence often occur slowly, as groundwater enlarges cavities in soluble rocks until they collapse, or as tectonic forces shift and lower entire crustal blocks (Kratzsch, 1983; Chaussard et al., 2013). In mining areas, the effect is more direct. Removing ore or coal disturbs the stress balance in the surrounding rock mass, prompting deformation that may eventually extend to the surface. The scale and rate of movement depend on factors such as mining depth, panel geometry, extraction method, rock mass stiffness, and the stratigraphy of the overburden (Whittaker & Reddish, 1989; Li et al., 2020; Fan et al., 2021).

As mining progresses, the ground above responds in a sequence of changes. The immediate roof may cave into the void, the layers above may bend or arch, and weaker beds can fracture or separate. Over time, the loosened mass compacts, creating a subsidence trough at the surface (Kratzsch, 1983; Whittaker & Reddish, 1989).

Figure 2.1 provides a simplified conceptual view of the physical mechanism that leads to mining-induced surface subsidence. When an underground excavation or convergence volume ΔV forms at depth H, stresses in the surrounding rock mass redistribute and deformation begins to propagate upward through the overburden within the influence zone defined by the angle β. As this deformation reaches the surface, it produces a characteristic subsidence trough S(r) with a maximum vertical settlement S_{max} at the center and an influence radius R marking the lateral extent of detectable movement. This “cause-process-result” sequence follows the general interpretation presented in Jiang et al. (2020, Fig. 1), but is adapted here to the notation and analytical framework used in this thesis.

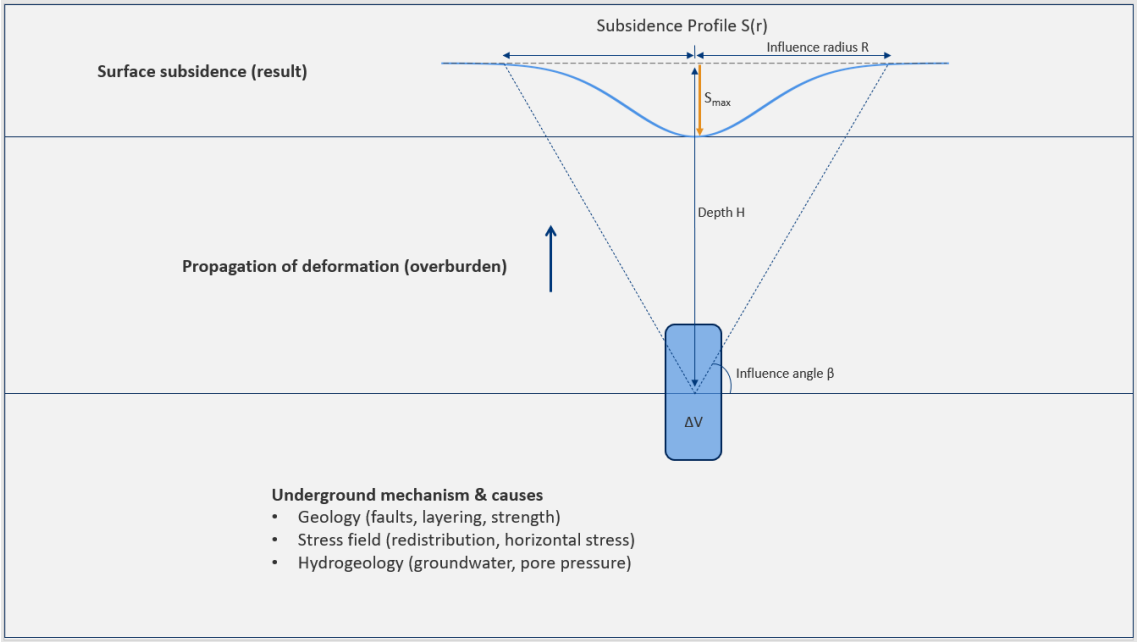

Figure 2.1 Conceptual diagram illustrating the underground convergence volume ΔV, the influence angle β, the depth H, and the resulting surface subsidence profile S(r).

Movement within this trough can be described in terms of vertical displacement, surface tilt, curvature, and horizontal movement either toward or away from the excavation (Peng, 2019; Wang et al., 2018). The nature of this progression varies: in some cases, movement is gradual and continues long after extraction has finished; in others, the collapse of overburden leads to a sharp, sudden drop.

The time frame over which subsidence develops depends on geological, hydrological, and operational conditions. Progressive subsidence, as seen in longwall mining or aquifer compaction, results from the slow upward migration of voids and the gradual redistribution of stresses (Whittaker & Reddish, 1989; Peng, 2019). In contrast, sudden subsidence is linked to abrupt roof or pillar failure in mines or the collapse of a karst cavity, producing visible ground movement within hours or days (Bell et al., 2000). The delay between underground excavation and surface change can vary considerably, influenced by the stiffness of the overburden, the rate of extraction, and the presence of groundwater (Peng, 2020; Li et al., 2020).

The consequences of subsidence can be severe. Buildings may crack or tilt, transport networks can deform, and buried pipelines may shift or rupture (Kratzsch, 1983; Bell et al., 2000). Water systems can also be affected, with altered drainage patterns, reduced aquifer capacity, and increased flooding risk (Galloway & Burbey, 2011; Chaussard et al., 2013). In ecological terms, soil degradation, wetland loss, and habitat disruption are common outcomes (Herrera et al., 2021). These impacts have made accurate prediction and continuous monitoring a priority in both mining and urban planning.

The study of mining-induced subsidence has a long history. Early nineteenth-century investigations in Belgium connected shallow coal workings to surface damage, and Gonot (1858) recognized the role of seam depth and inclination in shaping subsidence patterns. Henri Fayol later formalized the concept of collapse, transition, and surface deformation zones, which continues

to be used in engineering assessments. In Britain, the “angle of draw” was adopted to estimate the horizontal reach of surface movement, while in Germany analytical methods such as the influence function method were developed (Kratzsch, 1983). Through the twentieth century, empirical relationships and geometric rules were refined into analytical models, and later into numerical simulations using finite and discrete element methods (Li et al., 2020). In recent decades, advances in remote sensing have transformed monitoring practice. InSAR now allows displacement to be detected with millimeter precision across entire mining districts, providing valuable input for the estimation of subsidence model parameters from satellite line-of-sight data (Wang et al., 2018; Herrera et al., 2021).

Tilt and Horizontal movement

While vertical subsidence is the most visible sign of mining-induced ground movement, tilt and horizontal displacement are equally important for understanding the complete deformation field and assessing risks to infrastructure (Kratzsch, 1983; Whittaker & Reddish, 1989). In many cases, differential slopes or lateral shifts can cause greater structural damage than vertical settlement, particularly for long-span structures such as railways, pipelines, and industrial foundations (Peng, 2019). Usually, vertical displacement by itself causes little direct damage to the surface. Most damage results from the tilting and lateral movement of the overlying strata, which accompany the overall subsidence of the ground (Witkowski et al., 2021).

In mining areas, subsidence develops from the downward movement of rock layers above the extracted seam and the upward redistribution of stresses from the excavation voids. These processes create continuous surface deformations described by vertical subsidence, tilt, curvature, horizontal displacement, and horizontal strain. Among these, horizontal strain is particularly critical for assessing risks to surface structures, as it is highly sensitive to local terrain and geological heterogeneity (Witkowski et al., 2021).

Tilt represents the gradient of vertical subsidence and reflects how steeply the surface is inclined. It is dimensionless but commonly expressed in millimeters per meter as a threshold indicator for structural safety (Whittaker & Pasamehmetoğlu, 1981). Horizontal displacement describes the lateral movement of surface points relative to their original positions, typically directed toward the center of the subsidence trough, although outward movement may occur near trough edges depending on excavation geometry and overburden response (Wang et al., 2018).

Within the influence function method, vertical subsidence is often represented by a Gaussian-type profile. For a quasi-elementary excavation of volume V, and assuming a homogeneous, isotropic rock mass, Knothe's theory describes surface subsidence as (Tajduś et al., 2018):

$$S(r) = \frac{a\,V}{R^2}\ \exp(-\pi\ \frac{r^2}{R^2})$$

Where a is the subsidence factor, R is the radius of the main influence range, and r is the horizontal distance from the cavity axis.

The tilt of the elementary trough is obtained by differentiation:

$$T(r) = \frac{\partial S(r)}{\partial r} = -2\,\pi\ \frac{r}{R^2}\ S(r)$$

Classical Avershin–Budryk–Knothe theory links tilt to horizontal displacement by a proportional law:

$$U(r) = -B \cdot T(r)$$

Where B is the horizontal movement constant.

In two dimensions, this extends to directional components (Yang et al., 2022):

$U_E = -B \cdot T_E, \qquad U_N = -B \cdot T_N,$

with the east–west (T_E) and north–south (T_N) tilt components are defined as:

$$T_E = \frac{\partial S}{\partial x} = -\frac{2\pi x}{R^2} S_{max} \exp(-\pi \frac{r^2}{R^2})$$

$$T_N = \frac{\partial S}{\partial y} = -\frac{2\pi y}{R^2} \cdot S_{max} \exp(-\pi \frac{r^2}{R^2})$$

Where, S_{max} is the maximum vertical subsidence at the trough center and $r = \sqrt{x^2 + y^2}$.

Empirical monitoring has confirmed the proportionality $U = -B \cdot T$ in various mining fields (Sroka & Schober, 1987; Sroka et al., 2017). The same methodology links horizontal strain and vertical curvature K:

$$\varepsilon = -B \cdot K$$

From a structural-risk perspective, horizontal strain is the most critical deformation parameter, making accurate determination of B essential (Tajduś et al., 2018). When the horizontal movement factor follows the standard form $B = \lambda \cdot R$, displacement can be written as

$$\mathrm{U(r)} = 2\,\pi\,\lambda\,\frac{r}{R}\,S(r)$$

Which rearranged to

$$\frac{U(r)}{S(r)} = 2\,\pi\,\lambda\frac{r}{R}$$

This shows that horizontal displacement and vertical subsidence are linearly related across the entire subsidence trough, a relation confirmed both experimentally and in situ (Tajduś et al., 2018).

Witkowski et al. (2021) introduced a method to compute the horizontal strain tensor from InSAR by decomposing LOS displacement into vertical and azimuthal components. Earlier horizontal-strain models relied on empirical links to mining geometry or other subsidence measures, which worked reasonably well on flat terrain with uniform overburden but often underpredicted strain in irregular

ground conditions. Statistical models have also been applied, estimating exceedance probabilities for strain limits from monitoring records, yet their transferability beyond sites with similar conditions remains limited. Direct measurements with electrolevels or GNSS can capture directional strains, but their magnitudes vary strongly across a site and are constrained by sparse station coverage.

InSAR overcomes several of these limitations by providing high-density measurements that are unaffected by cloud cover. However, as a single-geometry technique it only yields displacement in the satellite's line of sight. To reconstruct three-dimensional motion, three strategies are commonly applied (Witkowski et al., 2021):

1. Single-geometry LOS combined with a deformation model, which requires reliable external inputs;
2. Multi-pass LOS with MAI or offset tracking, which suffers from reduced accuracy for slow deformation;
3. InSAR–GNSS fusion, which is limited by the availability of dense GNSS networks.

Despite these advances, existing methods often struggle to achieve both high accuracy and spatial resolution, particularly in urban mining areas where reliable strain mapping is most critical. Witkowski et al. (2021) addressed this gap with a double-geometry InSAR strategies. Their method assumes that horizontal displacement is proportional to the first derivative of vertical displacement a principle long used in subsidence theory and in analogous cases such as landslides and glacier flow. By applying geostatistical filtering to LOS data, they reduced noise and stabilized spatial derivatives, enabling solid computation of the horizontal strain tensor from the processed deformation field.

In this thesis, both approaches are applied. Analytical influence functions are used to simulate tilt and horizontal displacement from synthetic vertical

subsidence data, while the proportional law is used as an independent check to validate results against measurement-derived values.

2.2 InSAR-Based Monitoring of Subsidence

Interferometric Synthetic Aperture Radar (InSAR) is a remote sensing technique that detects ground surface deformation by comparing phase differences between two radar images acquired at different times from nearly identical satellite positions. It is particularly effective for monitoring mining-induced subsidence due to its ability to measure millimeter-scale movements over wide areas with high spatial resolution (Massonnet & Feigl, 1998).

InSAR measures displacement in the satellite's line-of-sight (LOS) direction, which combines vertical and horizontal components into a single projection. Due to satellite orbit geometry, the technique is most sensitive to vertical and east–west movements, while north–south displacements are poorly constrained (Zebker & Villasenor, 1992). This anisotropy makes it difficult to reconstruct the complete three-dimensional (3D) deformation field from single-track observations.

In general, the projection of three-dimensional ground displacement (W, N, E) onto the radar line-of-sight is expressed as (Yang et al., 2022):

$$d_{LOS} = W\cos(\theta) + N\sin(\theta)\cdot\cos(\alpha) - E\sin(\theta)\cdot sin(\alpha)$$

where, W is vertical, N is north, and E is east displacement, θ is the incidence angle, and α is the satellite heading. This form shows the limitation of radar geometry, as north–south movements are not well constrained.

Several perspectives have been developed to address this limitation. A common method is to combine ascending and descending orbit acquisitions, which provide different viewing angles of the same area. Joint analysis of their LOS displacements enables estimation of vertical motion and one horizontal

component along the azimuth-look direction (Colesanti et al., 2003; Witkowski et al., 2021). This can be expressed as a two-equation system:

$$\begin{bmatrix} d_{los}^{asc} \\ d_{los}^{desc} \end{bmatrix} = \begin{bmatrix} cos\ \theta^{asc} & \frac{sin\ \theta^{asc}}{cos\ \Delta\alpha} \\ cos\ \theta^{desc} & sin\ \theta^{desc} \end{bmatrix} \begin{bmatrix} d_v \\ d_{ALD} \end{bmatrix}$$

where, d_v is the vertical displacement and d_{ALD} is the horizontal component along the azimuth-look direction.

This decomposition recovers two displacement components but does not resolve the full three-dimensional displacement field (d_x , d_y , d_z) without external constraints such as GNSS measurements or additional orbits (Witkowski et al., 2021).

More advanced methods integrate multiple geometries or GNSS data to improve full 3D decomposition (Fuhrmann & Garthwaite, 2019; Witkowski et al., 2021). When only single-track data are available, vertical displacement is sometimes approximated by dividing the LOS measurement by the cosine of the incidence angle. However, this simplification neglects horizontal motion and introduces bias, especially in mining areas where lateral displacement and tilt are significant (Yang et al., 2016; Wang et al., 2018). To address this, Yang et al. (2016) proposed an improved inversion model linking LOS observations directly to Probability Integral Method (PIM) parameters. Their procedures, which employed a genetic algorithm with gross error elimination (GAGEE), allowed joint prediction of vertical and horizontal displacements and reduced reliance on oversimplified assumptions.

Time series InSAR techniques have further strengthened mining deformation monitoring. Persistent Scatterer Interferometry (PSI) and the Small Baseline Subset (SBAS) techniques reduce errors caused by atmospheric delays, temporal decorrelation, and phase unwrapping. PSI is especially effective

in urban and mining environments where man-made structures provide stable reflectors (Ferretti et al., 2001), while SBAS is more suitable for areas dominated by distributed scatterers such as natural ground surfaces (Hooper et al., 2004). Recent SBAS-InSAR applications in coal mining regions have demonstrated its effectiveness for capturing both the magnitude and spatial distribution of mining-induced ground deformation (Xie et al., 2024). However, PSI requires persistent stable scatterers, which may be sparse in rural or undeveloped mining areas, and SBAS performance decreases when long-term coherence is weak. Beyond monitoring, InSAR has been increasingly applied for predictive modeling. Wang et al. (2017, 2018) combined InSAR with the probabilistic integral method to refine subsidence forecasting, showing that coupling satellite data with classical models enhances site-specific accuracy. Witkowski et al. (2021) further demonstrated that high-resolution InSAR can be used to derive horizontal strain tensors by decomposing LOS data into vertical and azimuthal components, capturing deformation sensitivity to local geological conditions.

InSAR is applied not only as a monitoring technique but also as a system for parameter estimation. Synthetic line-of-sight (LOS) datasets are generated from forward subsidence models using defined satellite geometry, which allows controlled testing of inversion methods. This setup connects classical influence function theory with modern InSAR observations. By incorporating tilt and horizontal displacement into the synthetic modeling, the approach provides a more reliable basis for inferring subsidence parameters than methods restricted to vertical subsidence alone.

2.2.1 InSAR-Based Parameter Inversion of the Probability Integral Method (PIM)

The Probability Integral Method (PIM) is one of the most widely applied techniques for predicting mining-induced subsidence. It represents vertical displacement, tilt, curvature, and horizontal movement as integrals of influence functions over the mined-out area, providing closed-form solutions for the

expected deformation (Kratzsch, 1983; Whittaker & Reddish, 1989). Core model parameters such as the subsidence factor, the radius of main influence, and the horizontal movement constant are generally site-specific and require calibration against field measurements.

Early studies combined PIM with Differential InSAR (D-InSAR) to improve spatial prediction accuracy. Fan et al. (2014) applied radar-derived displacement fields to refine the influence radius and subsidence coefficient, achieving closer agreement with observed settlement profiles in coal mining areas.

To capture the temporal evolution of subsidence, Yang et al. (2016) introduced a logistic time function within the PIM design, calibrated using D-InSAR sequences. Their method successfully reproduced progressive deformation with strong agreement to leveling observations ($R^2 > 0.9$). Later studies extended this idea with more flexible time functions. Zhang et al. (2022) proposed a piecewise-optimized Knothe function, while Hou et al. (2022) integrated an Improved PIM with the Gompertz function (IPIM–G). The latter achieved better fitting in steep-gradient zones, reducing edge errors and improving prediction reliability compared to earlier models.

Hybrid approaches were also developed to address decorrelation in areas of large displacement gradients. Wang et al. (2020) combined D-InSAR with sub-band interferometry and offset-tracking, allowing PIM calibration in both coherent and incoherent regions. This improved basin-scale predictions, although the accuracy depended on the stability of pixel-tracking results.

Other researchers directly linked radar line-of-sight (LOS) observations with PIM parameters. Yang et al. (2016) formulated a projection equation that expresses the LOS signal as a linear combination of vertical, east–west, and north–south displacements, based on satellite geometry. Integrating this with PIM, they applied a genetic algorithm with gross error elimination (GAGEE) to jointly estimate subsidence parameters and predict both vertical and horizontal

displacements. Validation with synthetic and field data confirmed accuracy within a few centimeters.

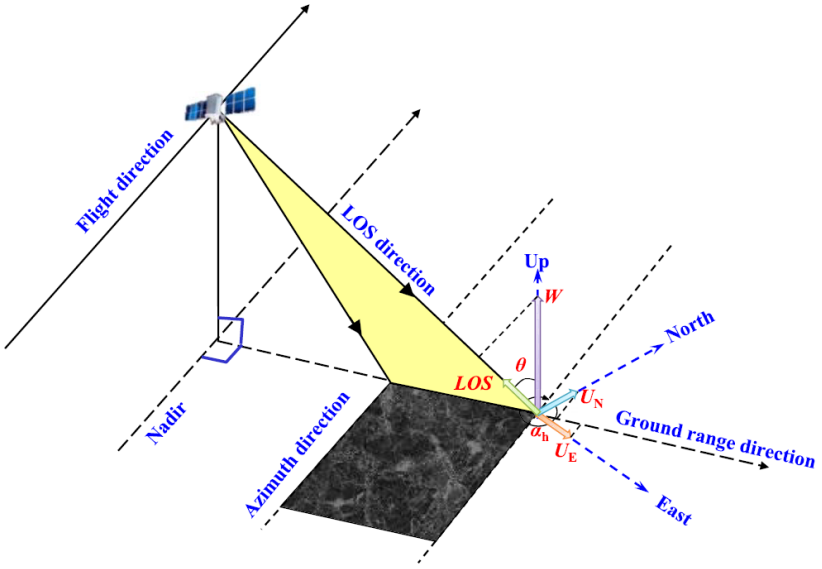

Figure 2.2 Projection of 3-D displacements onto the radar LOS. Adapted from Yang et al. (2016).

The LOS signal is composed of contributions from vertical and horizontal motion. The projection equation used to calculate LOS from simulated 3D displacement is:

$$d_{LOS}(x,y) = C_1 W(x,y) + C_2\, U_N(x,y) + C_3 U_E(x,y)$$

where,

W (x, y) – vertical displacement

U_N *(x, y)* – north-south horizontal displacement

U_E *(x, y)* – east-west horizontal displacement

θ – radar incidence angle

α_h - satellite azimuth angle (clockwise from North)

$C_1 = cos\theta,\ \ C_2 = -\sin\theta\cos\left(\alpha_h - \frac{3\pi}{2}\right),\ \ C_3 = -\sin\theta\sin\left(\alpha_h - \frac{3\pi}{2}\right).$

Building on this concept, Wang et al. (2018) employed Simulated Annealing (SA) optimization to recover the full set of PIM parameters from single-LOS D-InSAR data. By projecting model-based 3D displacements into LOS space and minimizing residuals, they obtained relative errors below 2% and RMSE values under ±1 mm. This demonstrated that single-track InSAR can provide reliable parameter inversion when combined with physically based deformation models.

Overall, these studies show a clear evolution from simple spatial adjustments of PIM parameters with D-InSAR (Fan et al., 2014) to more advanced approaches that incorporate time functions (Yang et al., 2016; Zhang et al., 2022; Hou et al., 2022), hybrid InSAR techniques (Wang et al., 2020), and full LOS-projected inversion models (Yang et al., 2016; Wang et al., 2018). While progress has been made, challenges remain in simultaneously capturing spatial and temporal deformation characteristics, particularly at the edges of subsidence basins.

2.2.2 Influence of Satellite Viewing Geometry on Parameter Estimation

InSAR is more sensitive to vertical ground motion than to horizontal displacement, particularly in the north–south direction. This is a direct result of near-polar satellite orbits. For example, with ALOS PALSAR (θ = 38.74°, α_h = 349.82°), the projection of ground displacement into the radar line-of-sight (LOS) produces a sensitivity vector of approximately (0.78 (Up), 0.16 (North), −0.60 (East)) (Yang et al., 2016). Vertical motion therefore dominates the LOS signal, while north–south contributions are comparatively small.

Yang, Xu, Li, Wu, and Zhu (2022) proposed a point-wise method for estimating three-dimensional mining displacements from LOS measurements using only three prior parameters: the horizontal movement constant (b), mining depth (H), and the tangent of the major influence angle (tan β). The LOS displacement was modeled as an S-shaped curve fitted with a Weibull function, while a Kalman filter accounted for residual fluctuations. Horizontal components

were derived under the assumption that they are proportional to the gradient of vertical subsidence, consistent with classical influence function theory. Applied in the Datong coalfield, this procedures achieved RMSEs of 0.006 m (vertical), 0.005 m (east), and 0.011 m (north) compared with GPS data. Sensitivity tests showed that reliable results were obtained even when prior parameters varied by up to ±43%, demonstrating that reliable estimates can be achieved with empirically assigned values. These findings are highly relevant to the present research, which also relies on projecting vertical and horizontal displacements into LOS space and testing parameter sensitivity in a controlled environment.

Multi-track InSAR provides an additional means of improving displacement estimation. By combining data from ascending, descending, or side-looking passes, overlapping coverage can be used both to stabilize measurements and to decompose LOS displacements into vertical and horizontal components. A well-documented example is the Groningen gas field in the Netherlands, where six ERS tracks were connected to reduce inter-track inconsistencies. After datum alignment, velocity variations decreased to below 1 mm/year in about 70 percent of persistent scatterer clusters (Ketelaar, 2009). The advantage of multi-track strategies is their ability to separate vertical displacement and one horizontal component aligned with the satellite's flight direction, an option unavailable with single-track InSAR (Witkowski et al., 2021).

Although time series methods such as PSI and SBAS mitigate atmospheric and decorrelation noise (Ferretti et al., 2001; Hooper et al., 2004), they cannot overcome the geometric limitation of single-track InSAR. This is why projection-based structure, such as those by Yang (2016, 2022) and Wang et al. (2018), are essential. They allow full 3D deformation to be inferred from LOS data when supported by physical models like the Probability Integral Method (PIM). The current thesis builds on this principle by applying a Gaussian influence function to generate synthetic vertical and horizontal displacements, projecting

them into LOS space, and then testing inversion performance under varying parameter conditions.

2.2.3 Challenges and Implications for Modeling

Although InSAR provides dense and precise measurements of surface deformation, several limitations affect its direct application in subsidence analysis. The technique is most sensitive to vertical and east–west movements, while sensitivity to north–south displacement is weak due to satellite orbit geometry (Zebker & Villasenor, 1992; Yang et al., 2016). Phase decorrelation also becomes significant in mining areas with large displacement gradients, leading to signal loss in zones near active panels (Wang et al., 2020). Atmospheric delays, temporal decorrelation, and phase unwrapping errors further complicate the interpretation of single interferograms (Ferretti et al., 2001; Hooper et al., 2004).

Time series InSAR methods such as PSI and SBAS mitigate part of these limitations, but challenges remain in reconstructing full three-dimensional displacements and in reliably estimating horizontal strain in complex geological settings (Witkowski et al., 2021). These constraints highlight the need to integrate InSAR observations with analytical or empirical modeling approaches. By including InSAR into established subsidence prediction models such as the Probability Integral Method (PIM), it becomes possible to both improve parameter estimation and extend predictions beyond observed deformation. These developments show that InSAR achieves its best results when combined with analytical subsidence models. Previous work has focused mainly on the Probability Integral Method (PIM). The influence function method, including its Gaussian formulation, provides an equally suitable basis for projecting vertical and horizontal displacements into the satellite line-of-sight. This thesis applies that principle by using a Gaussian influence function to generate synthetic subsidence fields, convert them into LOS geometry, and test parameter estimation performance under controlled conditions.

2.3 Approaches to Subsidence Modeling

The prediction of mining-induced ground deformation has been addressed through three main categories of modeling strategies: empirical, numerical, and analytical. Each reflects a different stage in the historical development of subsidence modeling, shaped by the availability of monitoring data, computational tools, and engineering requirements (Kratzsch, 1983). The choice of method depends on the objective of the study, the geological conditions, and the availability of data. Empirical methods remain useful for rapid predictions, while physics-based analytical and numerical models are applied to more detailed case studies.

2.3.1 Empirical Methods

Empirical subsidence prediction was common before physical and computer-based models were introduced. Kratzsch (1983) identifies seven principal approaches used across Europe.

The Angle-of-Intersection method uses seam dip and strike diagrams to outline subsidence trough boundaries. The British Profile-Curve Method represents the trough using three values: maximum, half-maximum, and marginal subsidence, based on levelling surveys and expressed in nomograms. The Russian Profile-Curve Method uses a sinusoidal curve, making it more mathematical but less adaptable to irregular deformation. The Polish Method applies a power-law function derived from flat stratified terrains. The Hungarian Method uses an exponential decay related to panel length and subsidence extent. The Programmed Profile-Curve Method, developed in the 1960s, combined empirical parameters with seam geometry for use in early computer systems. The Empirical Integration-Grid Method divides the mined area into cells and calculates the effect of each cell on surface points, adjusting inconsistencies with linear algebra techniques. These methods were effective when levelling data

were available, but their reliance on fixed shapes and site-specific fitting limited their wider application.

Reviews by Bell et al. (2000), Cai et al. (2019), and Arif et al. (2018) emphasize that while empirical methods were practical and widely applied in coal mining regions, their predictive ability is limited outside the range of conditions from which they were derived. Their reliance on levelling surveys also restricted spatial coverage and temporal resolution, which constrained their application in modern monitoring contexts. Today, empirical methods are primarily of historical interest or used for rapid approximations where detailed data are unavailable.

2.3.2 Numerical Methods

Numerical models represent a further step toward physical realism by explicitly simulating stress–strain responses of the rock mass. Finite Element Method (FEM) and Boundary Element Method (BEM) models can account for stratigraphy, material heterogeneity, and non-linear deformation (Kratzsch, 1983; Whittaker & Reddish, 1989). These methods are well established in geomechanics and have been applied to subsidence prediction where sufficient geological data are available.

Karmis et al. (1980s–2000s) demonstrated applications of numerical modeling in U.S. coalfields, showing their ability to capture site-specific effects. Li et al. (2020) used inverse numerical models to estimate interbed properties and transmissivity from subsidence and drawdown data. Liu and Zhang (2021) applied Kalman filter-based strain models to time series InSAR, demonstrating integration of numerical methods with satellite monitoring. Samsonov and Tiampo (2011, 2013) developed optimization frameworks combining D-InSAR with numerical adjustments, bridging analytical inversion with numerical simulation.

Although computationally intensive and data-demanding, numerical models are essential where complex geology or irregular layouts make analytical solutions insufficient. Their integration with InSAR offers promising opportunities for

subsidence models that are both physically grounded and observation-constrained.

2.3.3 Analytical Model

Analytical models describe the transfer of deformation from an underground excavation to the surface through closed-form mathematical expressions. Unlike empirical methods, which rely on curve fitting, or numerical models, which require iterative computation of boundary conditions, analytical techniques provide simplified but physically interpretable relationships between mining geometry, overburden response, and surface subsidence (Kratzsch, 1983; Whittaker & Reddish, 1989). They are particularly suitable when excavation geometry can be idealized, such as longwall panels or circular cavities.

These models allow derivation of vertical subsidence, tilt, curvature, and horizontal movement using relatively few parameters. Their efficiency and clarity have ensured their continued use in engineering design and monitoring, particularly when combined with modern remote sensing such as InSAR. Among analytical models, the influence function method has become the most widely applied due to its balance between physical interpretability and computational practicality.

2.4 Influence Function Method

The influence function method is the most widely applied analytical method to subsidence prediction. It represents surface displacement as the superposition of contributions from small excavation elements distributed across the mined area (Kratzsch, 1983). The mined area is divided into small units, and the displacement at any surface location is calculated as the superposition of their weighted contributions. The weighting function determines how influence decreases with distance from the excavation. Knothe (1953) first introduced an exponential influence function. Later studies demonstrated that Gaussian-type

kernels provided a better fit to observed subsidence profiles and improved analytical flexibility (Whittaker & Reddish, 1989).

From the vertical subsidence function, tilt and curvature can be obtained analytically through differentiation (Kratzsch, 1983). Horizontal displacement can be derived either from geometric relations or from volume conservation principles. This structure has made the influence function method attractive for both theoretical work and engineering design (Karmis et al., 1989).

Applications of the method have expanded beyond coal mining. Systematic developments were made by Sroka and Schober (1982, 1987), who expanded the theory for mining applications, and later extended by Sroka (2017) to include salt cavern fields. Field validation and the implementation of the method in tools such as SubCav© confirmed its practical relevance. More recent work by Babaryka and Benndorf (2023, 2025) focused on subsidence above salt caverns used for energy storage. Their 2023 study compared existing prediction methods and demonstrated that accounting for cavern convergence and asymmetric deformation significantly improves reliability. Building on this, their 2025 publication introduced a new influence-function-based formulation that incorporates asymmetry and shape flexibility. Application to case studies from northern Germany showed improved agreement with monitoring data compared to classical Gaussian models. These contributions underline the continued development of influence function methods and their adaptability to different geological and mining contexts.

2.4.1 Gaussian Formulation

A common form of the influence function is the Gaussian kernel, which produces a symmetrical subsidence trough and allows explicit derivation of subsidence and its derivatives. The vertical subsidence is given by:

$$S(r) = S_{max} \cdot \exp(-\pi \cdot \frac{r^2}{R^2})$$

where, $S(r)$ is the subsidence at horizontal distance r from the excavation center, S_{max} denotes the maximum subsidence directly above the cavity center, and R represents the radius of influence, typically dependent on cavity depth and angle of draw.

From this function:

- Tilt is obtained as the first derivative of S(r) with respect to r.
- Curvature is derived as the second derivative (Whittaker & Reddish, 1989).
- Horizontal displacement U(r) can be calculated from geometric relations or from volume conservation principles (Kratzsch, 1983; Sroka, 2017).

The Gaussian formulation remains widely applied because it balances computational simplicity with physical interpretability and has been validated against field measurements (Kratzsch, 1983; Whittaker & Reddish, 1989). Compared with Knothe's exponential kernel, it provides a closer representation of observed troughs and has been successfully used in both coal and salt mining contexts.

A further advantage of the Gaussian approach is its straightforward integration with satellite-based monitoring. Since vertical and horizontal displacement components can be derived analytically, they can be projected into the satellite line-of-sight geometry required for parameter estimation. This connection between influence function models and InSAR observations is explored further in the subsequent chapter on InSAR-based subsidence prediction.

2.5 Parameter estimation techniques

Parameter estimation is essential in subsidence prediction because analytical and empirical models require calibration to field or satellite data before they can provide reliable results (Kratzsch, 1983; Whittaker & Reddish, 1989). Early methods relied on deterministic fitting, most often least squares adjustment (Koch, 1999), while more recent developments introduced probabilistic frameworks such as Bayesian inference (Gelman et al., 2004) and sequential updating methods based on Kalman filtering (Kalman, 1960; Koch, 1999; Kusche & Klees, 2002; Xu, 2010). These estimation methods have also been applied with InSAR data. For example, Ferretti et al. (2001) demonstrated how least squares can retrieve deformation rates from PSI time series. Yang et al. (2016) introduced a genetic algorithm methodology to directly invert Probability Integral Method parameters from LOS observations, and Wang et al. (2018) further refined this approach using simulated annealing for more accurate parameter estimation. The following subsections review least squares, Monte Carlo simulation, Bayesian inference, and sequential estimation, with emphasis on their application to subsidence prediction and InSAR monitoring.

2.5.1 Least Squares Methods

Least squares adjustment is one of the standard methods in geodesy and engineering. It estimates parameters by minimizing the squared differences between observations and model predictions, assuming normally distributed errors. The method provides the best linear unbiased estimator (BLUE) and forms the basis for error propagation and statistical testing (Koch, 1999). The method provides both point estimates and a variance–covariance matrix, which allows for error propagation and statistical testing.

In subsidence modeling, classical formulations such as those by Kratzsch (1983) and Whittaker & Reddish (1989) define the geometry of subsidence troughs but require calibration to field data. Parameters such as the subsidence

factor and angle of draw are usually fitted through least squares regression (Peng, 2019). In satellite geodesy, least squares also plays a central role. The Permanent Scatterers InSAR technique introduced by Ferretti et al. (2001) applies least squares to retrieve deformation rates while correcting for atmospheric and orbital effects. Colesanti et al. (2003) later extended this approach to landslide and tectonic monitoring. In mining context, Yang et al. (2016) demonstrated that least squares can be directly applied to LOS observations for the inversion of Probability Integral Method (PIM) parameters, thereby improving prediction reliability without relying on oversimplified cosine correction of vertical subsidence.

The strength of least squares is its simplicity and analytical clarity. However, it assumes Gaussian error distributions and provides single point estimates, which may underestimate uncertainty when geological or observational conditions are complex.

2.5.2 Monte Carlo Simulation

Monte Carlo methods estimate parameters by repeated random sampling from defined probability distributions. Instead of producing a single deterministic solution, they generate a distribution of possible outcomes that reflects uncertainty in the input parameters. In mining, Monte Carlo simulation has been applied to risk evaluation and mine planning, where uncertain parameters such as extraction ratio or angle of draw are propagated through models to assess variability in subsidence predictions (Avchar et al., 2024).

Monte Carlo methods are particularly useful for uncertainty analysis. Unlike Bayesian inference, however, they do not incorporate prior information or parameter correlations. Their value lies in quantifying how sensitive a model is to parameter uncertainty, which is directly relevant for subsidence prediction in heterogeneous geological conditions.

2.5.3 Bayesian and MCMC Methods

Bayesian inference estimates parameters by combining prior information with observational data. Instead of a single best estimate, it produces a posterior probability distribution that represents both the estimate and its uncertainty. Markov Chain Monte Carlo (MCMC) algorithms are commonly used to sample from the posterior, allowing complex problems to be solved where analytical solutions are not available. Bayes' theorem expresses this relation, where the posterior is proportional to the likelihood multiplied by the prior (Gelman et al., 2004).

Bayesian methods have been applied in several geodetic and remote sensing studies. Samsonov and Tiampo (2006) introduced a Bayesian optimization approach to combine D-InSAR and GPS data into three-dimensional displacement estimates. Their method was analytical, but it demonstrated how Bayesian reasoning can stabilize inversion. Burke and Minsley (2014) developed a trans-dimensional Bayesian MCMC algorithm for electromagnetic data, allowing both parameter values and model complexity to be treated probabilistically. More recently, Graves et al. (2023) applied Bayesian MCMC inversion to InSAR deformation time series, obtaining posterior distributions and credible intervals for reservoir parameters. These studies show how Bayesian inference has progressed from analytical solutions to full MCMC implementations, providing a system that explicitly accounts for uncertainty and parameter dependence, an advantage over deterministic or purely sampling-based techniques.

2.5.4 Sequential Estimation and Kalman Filtering

Least squares can also be extended into sequential estimation through the Kalman filter, which is a recursive form of least squares (Kalman, 1960; Koch, 1999). Instead of solving the full system whenever new data become available, the Kalman filter updates parameter estimates step by step. Each cycle predicts the state and its covariance forward in time and then corrects them using the new

observations. This prediction update structure makes the Kalman filter suitable for monitoring dynamic processes such as progressive subsidence measured in repeated InSAR acquisitions. Variants of the classical filter have been proposed to improve stability in practical applications. For example, improved Kalman filters introduce adaptive weighting and noise models to reduce sensitivity to errors in deformation monitoring (Kusche & Klees, 2002; Xu, 2010). In geodesy, Kalman filtering has been applied to gravity field estimation (Kusche & Klees, 2002) and GPS/INS integration (Xu, 2010). In this study, the Kalman filter is applied to synthetic LOS time series with an imposed Gaussian noise of 1 and 2mm standard deviation. This allows the sequential updating scheme to be tested under uncertain conditions, demonstrating how parameter estimates can be refined iteratively as new InSAR acquisitions become available.

2.5.5 Comparative Perspective

Least squares provides point estimates under Gaussian assumptions and supports error propagation analysis (Koch, 1999; Ferretti et al., 2001). Monte Carlo methods describe variability by random sampling and are used in mining and geomechanics where parameter uncertainty is significant (Avchar et al., 2024). Bayesian and MCMC approaches extend estimation by producing full posterior distributions that capture uncertainty and parameter dependence (Gelman et al., 2004; Graves et al., 2023). Kalman filtering applies least squares sequentially, which makes it suitable for dynamic monitoring with time-dependent data (Kalman, 1960; Kusche & Klees, 2002; Xu, 2010).

These methods show a progression in parameter estimation. Early approaches were deterministic, focusing only on best-fit solutions. Later methods introduced probabilistic approaches to quantify uncertainty, and sequential filtering methods were developed for real-time applications. This evolution is directly relevant for subsidence modeling, where both uncertainty and continuous monitoring must be addressed. In this thesis, weighted nonlinear least squares is adopted as the primary estimator, with Monte Carlo, Bayesian, and EKF tests

used as complementary tools to explore uncertainty and sequential updating in a controlled synthetic setup.

3 Methodology

3.1 Overview of the Modeling Framework

This study develops a physically based subsidence modeling and parameter-estimation framework designed to infer key ground-movement parameters - influence angle (β), horizontal - tilt factor (λ), and convergence rate (μ) - from satellite line-of-sight (LOS) displacement data. The workflow combines analytical influence-function theory with synthetic LOS simulation to evaluate the capability of inverse-estimation methods under controlled conditions (Kratzsch, 1983; Whittaker & Reddish, 1989; Sroka, Knothe, & Tajduś, 2017).

The deformation field above a subsurface excavation is assumed to be smooth and axisymmetric, governed primarily by the excavation geometry and depth. A Gaussian-type influence function describes vertical subsidence, from which horizontal displacement, surface tilt, and curvature are derived analytically. The resulting three-dimensional displacement field is projected into the LOS direction using the satellite incidence and azimuth angles. Gaussian noise ($\sigma \approx$ 1–2 mm) is added to emulate the uncertainty level typical of InSAR measurements (Hanssen, 2001; Ferretti, 2007; Crosetto, Monserrat, Cuevas-González, Devanthéry, & Crippa, 2016).

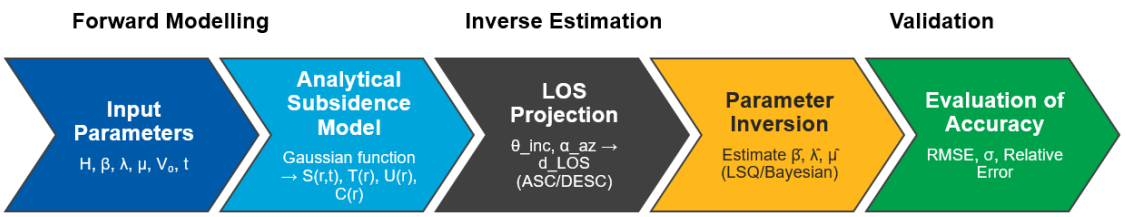

Figure 3.1 Summarizes the workflow, from parameter definition and analytical modeling to LOS projection, inverse estimation, and accuracy evaluation.

The following sections describe each component and its reproducible Python implementation.

All symbols used in the analytical formulation are defined in Table 3-1.

Table 3.1. Model parameters and notation

Symbol	Definition	Unit
S (r, t)	Vertical subsidence at distance r (positive downward)	m
$S_{max}(t)$	Maximum subsidence at trough center	m
r	Radial distance from the center	m
R	Radius of influence	m
T (r, t)	Tilt (slope of subsidence)	-
U (r, t)	Radial horizontal displacement (toward center)	m
H	Depth to cavity center	m
B	Horizontal – tilt coefficient, B = λR	m
λ	Horizontal – tilt factor	-
V_0	Initial/ reference cavity volume	m^3
ΔV(t)	Cumulative volume loss	m^3
μ	Convergence rate	yr^{-1}
β	Influence angle (from the vertical)	o
t	Time	yr
d_{Los}	Displacement in satellite line-of-sight direction	m
θ_{inc}	Radar incidence angle (from vertical)	o
α_{az}	Radar heading angle (azimuth clockwise from north)	o

All quantities are expressed in the East–North–Up (ENU) reference frame. Positive S indicates downward motion, and positive d_{LOS} indicates movement away from the satellite.

3.2 Analytical Formulation of Ground Movement

This thesis adopts a physically motivated, Gaussian-type influence function to represent ground-surface response to underground excavation. The formulation is axisymmetric, analytically differentiable, and parameterized by β, λ, and μ (Kratzsch, 1983; Whittaker & Reddish, 1989; Sroka et al., 2017).

3.2.1 Vertical Subsidence (radial form)

$$S(r,t) = S_{max}(t)\ \exp(-\pi\ \frac{r^2}{R^2}) \tag{3.1}$$

where, $S_{max}(t)$ is the maximum vertical settlement directly above the center, and R is the radius of main influence controlling lateral spread. The geometric relation to depth is

$$R\ =\ H\ cot(\beta) \tag{3.2}$$

with H the excavation depth and β the main influence angle (measured from the vertical). A larger β yields a narrower trough; a smaller β produces a wider bowl (Kratzsch, 1983; Whittaker & Reddish, 1989).

3.2.2 Volume - Subsidence Consistency

To ensure mass/volume consistency, the modeled settlement integrates to the time-dependent closure volume ΔV(t). For the kernel in Eq. (3.1), the axisymmetric area of influence is

$$A_{inf}\ = \int_0^{\infty} \exp(-\pi\ \frac{r^2}{R^2})\ 2\pi r\ dr\ =\ R^2. \tag{3.3}$$

Enforcing $\int S\,\partial A = \Delta V(t)$ gives

$$S_{max}(t) = \frac{a\Delta V(t)}{R^2}, \qquad S(r,t) = \frac{a\Delta V(t)}{R^2}\, exp\left(-\pi \frac{r^2}{R^2}\right). \tag{3.4}$$

where ΔV(t) is the cumulative volume of material removed or compacted by mining activity, and a is a dimensionless scaling constant typically set to 1. The exponential term defines the radial decay of subsidence from the center of excavation.

3.2.3 Two-Dimensional Surface (plan view)

For synthetic modeling on a horizontal plane, the vertical displacement at (x, y) relative to the center (x_c, y_c) is:

$$S(x,y,t) = S_{max}(t)\ \exp(-\pi\ \frac{(x-x_c)^2+(y-y_c)^2}{R^2}), \tag{3.5}$$

with the radial distance $r = \sqrt{(x-x_c)^2 + (y-y_c)^2}$. This 2-D form produces a smooth, radially symmetric subsidence surface well-suited for synthetic LOS projection in Section 3.3.

3.2.4 Tilt and Curvature

Tilt is the gradient of the subsidence profile with respect to distance and is given by:

$$T(r,t) = \frac{\partial S}{\partial r} = -2\pi\ \frac{r}{R^2}\ S(r,t)\ . \tag{3.6}$$

Curvature follows from the second derivative of S(r).

$$C(r,t) = \frac{\partial^2 S}{\partial r^2} = \left(\frac{4\pi^2 r^2}{R^4} - \frac{2\pi}{R^2}\right) S(r,t)\,. \tag{3.7}$$

Both measures are essential in practice: damage to surface infrastructure correlates strongly with slope and differential settlement, not only with the absolute trough depth (Whittaker & Reddish, 1989).

3.2.5 Horizontal Displacement

Horizontal movement is assumed proportional to the tilt (Avershin's law):

$$U(x,t) = -B\,\nabla S(x,t), \tag{3.8}$$

which, in radial form with positive direction towards the trough center, gives

$$U(r,t) = -BT(r,t) = -B\,\frac{dS}{dr} = \mathrm{B}\,2\,\pi\,\frac{r}{R^2}\,S(r,t). \tag{3.9}$$

To enable comparison across geometries, we write B=λR, where λ is a dimensionless horizontal–tilt factor. The radial profile $U(r) \propto r\,exp\left(-\pi\frac{r^2}{R^2}\right)$ attains its maximum at

$$r_{max} = \frac{R}{\sqrt{2\pi}}, \qquad U_{max} = \frac{\sqrt{2\pi}\,B}{e^{1/2}\,R}\,S_{max} \approx 1.5203\,\lambda\,S_{max}. \tag{3.10}$$

For completeness, the 2-D vector form used in the synthetic grids is

$$\nabla S(x,y,t) = -\frac{2\pi}{R^2}\,S(x,y,t)\begin{bmatrix} x - x_c \\ y - y_c \end{bmatrix}, \qquad U(x,y,t) = -B\nabla S(x,y,t)\,. \tag{3.11}$$

3.2.6 Time-Dependent Convergence

To represent the temporal development of deformation, the cavity is assumed to converge exponentially from its initial void volume V_0 at rate μ [yr^{-1}]:

$$\Delta V(t) = V_0\,(1 - e^{-\mu t}). \tag{3.12}$$

For short times ($\mu t \ll 1$), the first – order approximation is

$$\Delta V(t) \approx V_0\,\mu t, \tag{3.13}$$

while for multi-year horizons the exact form in Eq. (3.12) is retained. Using the volume–subsidence consistency from Eq. (3.4) and the area of influence $A_{inf} = R^2$ from Eq. (3.3), the maximum subsidence and the full radial profile become

$$S_{max}(t) = \frac{V_0}{R^2}(1 - e^{-\mu t}), \qquad S(r,t) = \frac{V_0}{R^2}(1 - e^{-\mu t})\exp(-\pi\ \frac{r^2}{R^2}). \tag{3.14}$$

Practical note. With an annual convergence rate of μ=0.01 (1%), the difference between the exact and linear expressions at t=1yr is below 0.5%, so Eq. (3.13) is adequate for single-epoch demonstrations; for longer time spans, Eq. (3.12) should be used.

Building on these expressions, the modeled vertical and horizontal displacements are projected into the satellite line of sight using the incidence and azimuth geometry of ascending and descending acquisitions, yielding synthetic LOS fields that serve as observations for the parameter-inversion procedure described in Section 3.3.

To illustrate the analytical expressions introduced above, Figure 3-2 shows theoretical one-dimensional profiles of vertical subsidence, horizontal

displacement, tilt, and curvature computed using the baseline parameter values later summarized in Table 3.2.

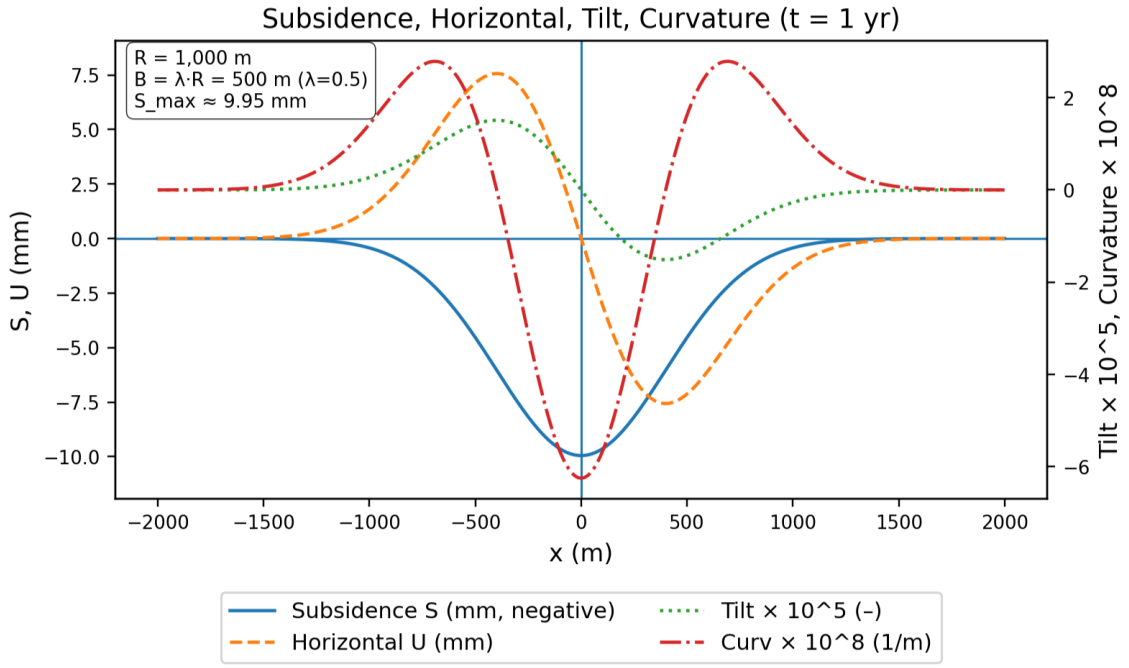

Figure 3.2 Theoretical 1-D profiles of subsidence, horizontal displacement, tilt, and curvature derived from the Gaussian influence-function model, and the effect of the horizontal–tilt factor.

Subsidence forms a symmetric trough centered above the excavation, while tilt and curvature peak at the shoulders where the slope is steepest. The lower plot demonstrates the influence of the horizontal–tilt factor λ; increasing λ amplifies horizontal displacement without changing the vertical trough shape.

The effect of λ on horizontal displacement is further shown in Figure 3-3. Increasing λ proportionally scales the horizontal movement U(r) while leaving subsidence, tilt, and curvature unchanged, confirming the analytical separation of vertical and horizontal deformation components.

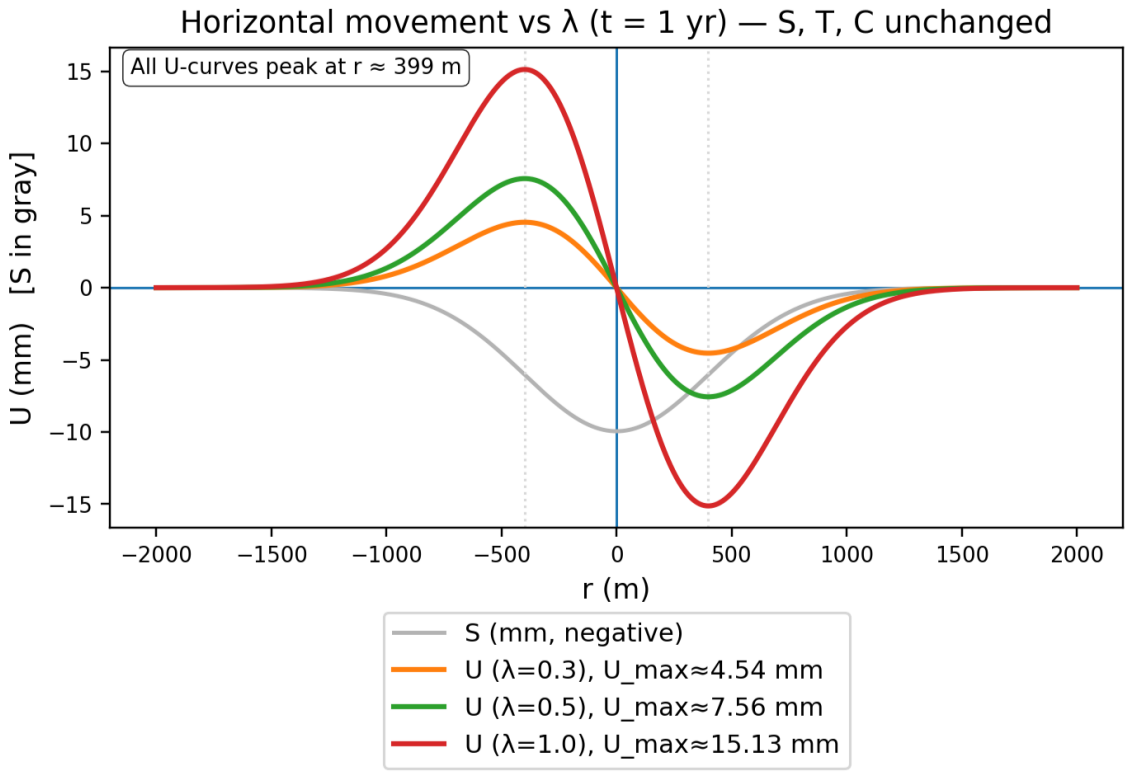

Figure 3.3 Effect of the horizontal–tilt factor λ on the horizontal displacement profile U(r) at t=1 yr.

All curves share the same subsidence S(r) (shown in gray). Larger λ values amplify horizontal movement according to B=λR but do not alter the shape of the vertical trough.

3.3 Line-of-Sight (LOS) Projection

3.3.1 Concept

Interferometric Synthetic Aperture Radar (InSAR) records the line-of-sight (LOS) displacement between the satellite and the ground surface.

Each acquisition is characterized by an incidence angle θ_{inc} (measured from the vertical) and an azimuth angle α_{az} (measured clockwise from north). Because the radar measures only motion along its viewing direction, the analytical displacement field from Section 3.2 must be projected onto this LOS vector.

The LOS displacement d_{LOS} is obtained by projecting the modeled three-dimensional ground-displacement vector $u = [U_x, U_y, S]^T$ onto the look vector $l = [l_x, l_y, l_z]^T$:

$$d_{LOS} = -u \cdot l. \tag{3.15}$$

By convention, $d_{LOS} > 0$ indicates motion away from the satellite (increase in range).

3.3.2 Projection geometry

For a satellite acquisition with incidence θ_{inc} and azimuth α_{az}, the unit look vector is expressed as

$$l = \begin{bmatrix} -sin\theta_{inc}\, sin\alpha_{az} \\ -sin\theta_{inc}\, cos\alpha_{az} \\ cos\theta_{inc} \end{bmatrix}. \tag{3.16}$$

Substituting the analytical displacement components from Section 3.2 gives

$$d_{LOS}(x,y,t) = S(x,y,t)\cos\theta_{inc} + U_x(x,y,t)\sin\theta_{inc}\, sin\alpha_{az} + \\ + U_y(x,y,t)\sin\theta_{inc}\, cos\alpha_{az} \tag{3.17}$$

In the axisymmetric case, the horizontal components follow

$$U_x = U(r,t)\frac{x-x_c}{r}, \quad U_y = U(r,t)\frac{y-y_c}{r}, \; r = \sqrt{(x-x_c)^2 + (y-y_c)^2}. . \tag{3.18}$$

Illustrative profiles (noiseless). Figures 3-4 and 3-5 visualize Eqs (3.15) – (3.18) for Sentinel -1 geometry (θ_{asc} = 33.5°, θ_{des} = 36.2°, $\Delta\alpha \approx 180°$) along a central section (y=0⇒r=|x|). The vertical term $-S\cos\theta_{inc}$ has the same sign in ASC and DES, whereas the horizontal terms reverse sign due to opposite azimuths; increasing the horizontal–tilt factor λ scales the LOS amplitude.

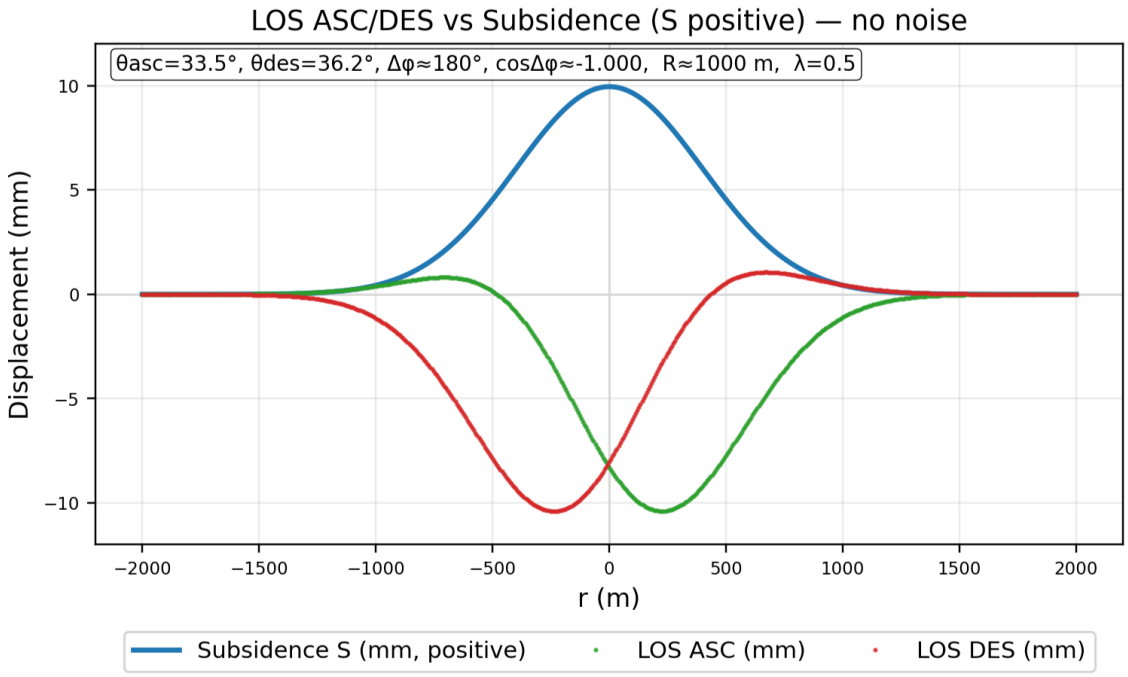

Figure 3.4 Comparison of LOS displacements from ascending (ASC) and descending (DES) geometries with vertical subsidence S(r) (no noise).

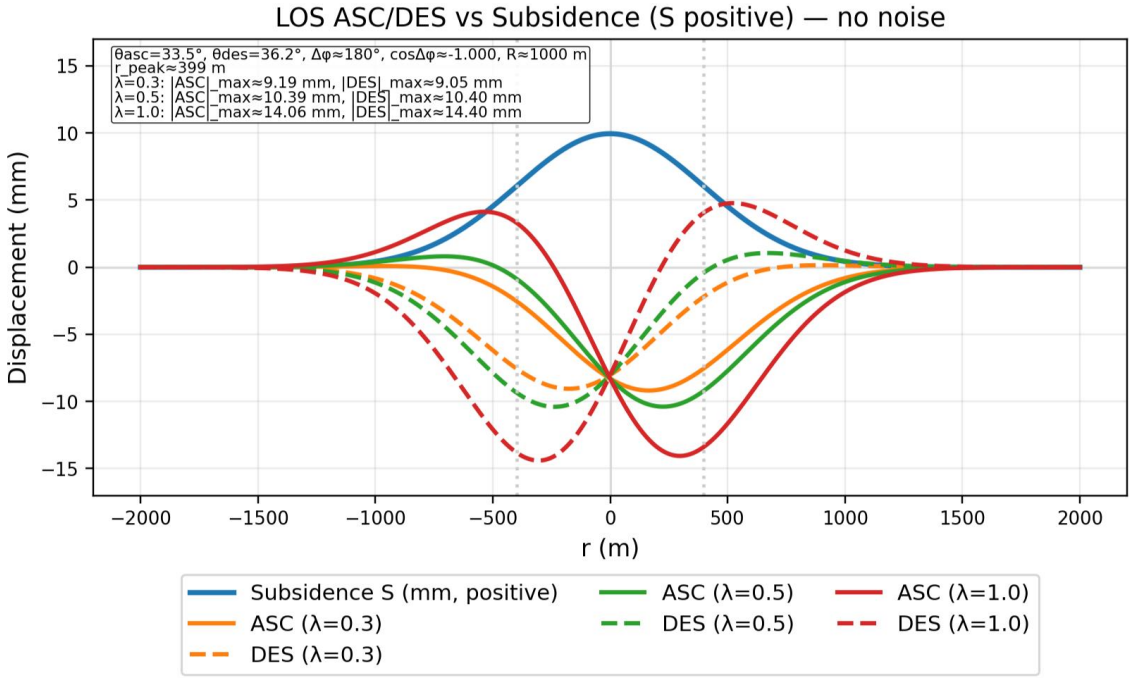

Figure 3.5 Effect of the horizontal–tilt factor λ on ASC/DES LOS profiles (no noise). The blue curve shows S(r) (positive downward).

Ascending and descending look geometry. For right-looking SAR systems such as Sentinel-1, ascending and descending passes observe the same scene from nearly opposite directions ($\alpha_{asc} \approx 76^{\circ}$; $\alpha_{des} \approx 256^{\circ}$; $\Delta\alpha \approx 180^{\circ}$). Incidence angles differ slightly $\theta_{asc} = 33.5^{\circ}$, $\theta_{des} = 36.2^{\circ}$). This complementary sensitivity enables joint estimation of β, λ, and μ from paired LOS observations.

Conventions

- Reference frame: East–North–Up (ENU).
- Incidence angle: θ_{inc} measured from vertical.
- Azimuth angle: α_{az} measured clockwise from north toward the look direction.
- Sign convention: $d_{LOS} > 0$ denotes motion away from the satellite.
- For Sentinel-1, the look azimuth equals the track heading ± 90°; when only headings are available, they are converted to α_{az} prior to applying Equations (3.16) – (3.17).

3.3.3 Implementation in the Synthetic Workflow

For each grid node (x_i, y_j):

1. Compute $S(x_i,y_j,t)$ and $U(r_{ij},t)$ from Eqs. (3.1) – (3.13).
2. Derive U_x, U_y using Eq. (3.18).
3. Apply Eq. (3.17) for both ascending and descending viewing geometries using the corresponding θ_{asc}, θ_{des}, and α_{asc}, α_{des}.
4. Add Gaussian noise to the simulated LOS: $d_{LOS}^{noisy} = d_{LOS} + \varepsilon$, $\varepsilon \sim N(0, \sigma^2)\ with\ \sigma \in \{1\ ,2\}\ mm$ to emulate InSAR measurement uncertainty. Figures 3-6 and 3-7 preview the effect along y =0.

This produces two synthetic LOS displacement fields, d_{LOS}^{asc} and d_{LOS}^{des}, that serve as observation datasets for the parameter-inversion procedure in Section 3.4–3.5.

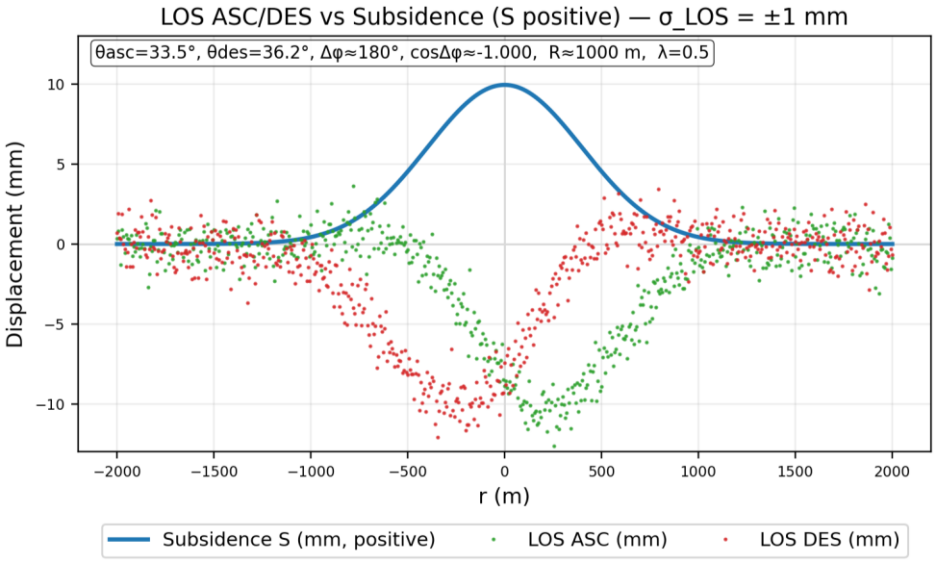

Figure 3.6 LOS profiles with additive Gaussian noise (σ_{LOS} = ±1 mm).

Noise corresponds to the typical precision of InSAR phase-based displacement measurements in highly coherent areas. The overall subsidence pattern remains clearly identifiable.

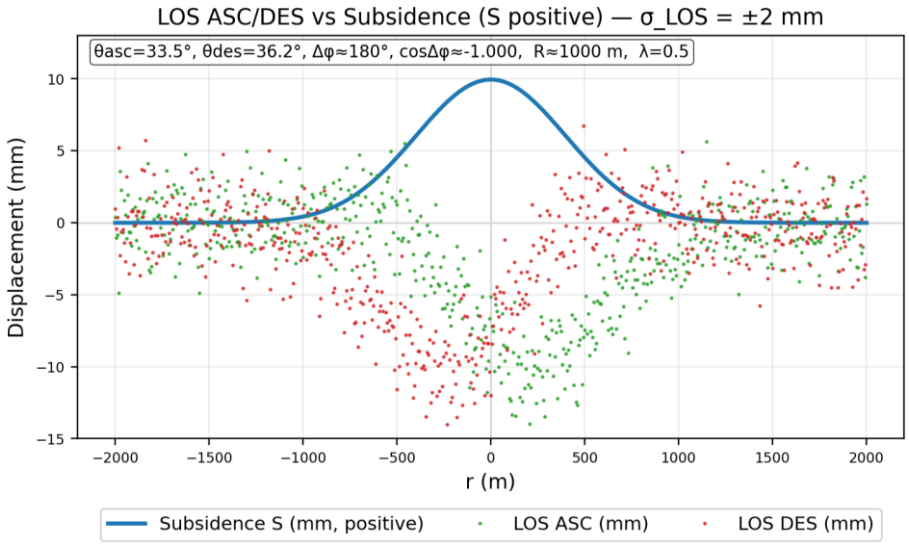

Figure 3.7 LOS profiles with additive Gaussian noise (σ_{LOS} = ±2 mm).

Higher noise levels reduce the signal-to-noise ratio but still preserve the characteristic LOS curvature, demonstrating the robustness of the synthetic forward model.

3.3.4 Remarks

- Complementarity: Ascending and descending passes differ mainly in azimuth; combining them increases sensitivity to horizontal motion while retaining vertical accuracy.
- Interpretation check: Pure vertical subsidence yields $d_{LOS}^{asc} \approx d_{LOS}^{des} < 0$; pure horizontal motion of equal magnitude but opposite direction produces opposite-sign LOS patterns.
- Scope: With only two viewing geometries, full 3-D decomposition is underdetermined; hence, inversion focuses on physically meaningful parameters β, λ, and μ within the analytical framework.

3.4 Synthetic Data Generation and Noise Model

3.4.1 Spatial Grid and Baseline Parameters

A two-dimensional modeling domain is defined on a regular Cartesian grid centered at (x_c, y_c). Each grid node is given by

$$x_i = x_c - L + i\Delta, \quad i = 0, \ldots, N_x - 1; \qquad y_j = y_c - L + j\Delta, \quad j = 0, \ldots, N_y - 1. \tag{3.19}$$

Where L is the half-width of the model domain and Δ is the spatial resolution.

The radial distance of each node from the model center is

$$r_{ij} = \sqrt{(x_i - x_c)^2 + (y_i - y_c)^2}. \tag{3.20}$$

Model symbols and notation used throughout Chapter 3 are summarized in Table 3-1, and the baseline parameter values adopted for the synthetic experiments are listed in Table 3-2. These parameters represent a realistic salt-cavern scenario and Sentinel-1 viewing geometry.

Table 3.2. Baseline parameters for synthetic experiments, observation geometry, and noise assumptions.

Symbol	Value	Unit	Note
H	1000	m	Realistic depth for a synthetic salt-cavern case; European practice often ~1,000–1,500 m. (Bérest & Brouard, 2003; Cyran, 2023).
β	45	°	Main influence angle (from vertical) chosen mid-range; we use R=Hcotβ. Classical ranges vary with geology.
V_0	1.0 x 10^6	m^3	Test cavern volume consistent with European storage practice (typical single-cavern volumes ~0.5–1.0 Mm^3). (Energy.nl, 2021).
μ	0.01	yr^{-1}	1 % per convergence is a practical, order-of-magnitude design/operation figure in cavern literature. (Brouard et al., 2013; Harati & Rezaei Gomari, 2025).
$S_{max}(t)$	~ 9.95	mm	Derived after a year with μ = 0.01. $S_{max} = \frac{10^6(1 - e^{-0.01})}{1000^2} = 9.95\, mm$
t	1	year	Single-epoch baseline for forward modeling and inversion; multi-epoch used later.
a	1	-	Volume-to-surface scaling in the Gaussian influence-function model (set to 1 for transparency). (Kratzsch, 1983).

λ	0.3 0.5 1.0	-	Dimensionless horizontal-movement factor; we also report B=λR. Values near 0.3 are typical; 0.5–1.0 for sensitivity. (Tandanand & Powell, 1991; Tajduś, 2015)
θ_{asc}	33.5	°	ASC incidence within Sentinel-1 IW range (~29–46° depending on subswath/incidence). (ESA, 2016)
θ_{desc}	36.2	°	DES incidence (different from ASC), reflecting real geometry. (ESA, 2016)
α_{asc}	76	°	ASC ground-range azimuth (clockwise from north); used as the horizontal reference ($\alpha_{ref} = \alpha_{asc}$). (Hanssen, 2001).
α_{des}	256	°	DES ground-range azimuth (approximately opposite to ASC at mid-latitudes). (Hanssen, 2001)
$\Delta\alpha$	180	°	Idealized opposite azimuth; enters the 2×2 system via $\cos\Delta\alpha$. (Witkowski et al., 2021)
σ (LOS noise)	± 1 and ± 2	mm	Additive LOS noise reflecting mm-level precision achievable with PS/PSI in high-coherence areas. (Ferretti et al., 2001; Crosetto et al., 2016).

3.4.2 Forward Fields and LOS Synthesis

At each grid node at (x_i, y_j), the vertical subsidence is calculated from Eq. (3.14) as

$$S_{ij}(t) = \frac{V_0}{R^2}(1 - e^{-\mu t}) \exp(-\pi \frac{r_{ij}^2}{R^2}). \quad (3.21)$$

and the radial horizontal displacement following the Avershin's law (Section 3.2.5) is

$$U(r_{ij}, t) = \mathrm{B}\, 2\pi \frac{r_{ij}}{R^2} S_{ij}(t), \quad (3.22)$$

The axisymmetric components of horizontal displacement in the East–North–Up (ENU) frame are:

$$U_{x,ij} = U(r_{ij}, t)\frac{x_i - x_c}{r_{ij}}, \qquad U_{y,ij} = U(r_{ij}, t)\frac{y_i - y_c}{r_{ij}}, \qquad \text{with } U_{x,ij} = U_{y,ij} = 0 \; at \; r_{ij} = 0. \tag{3.23}$$

For each satellite geometry (ascending and descending) defined by incidence θ_{inc} and azimuth α_{az}, the modeled LOS displacement is obtained from Eq. (3.17):

$$d_{LOS,ij} = -S_{ij}\cos\theta_{inc} + U_{x,ij}\sin\theta_{inc}\, sin\alpha_{az} + U_{y,ij}\sin\theta_{inc}\, cos\alpha_{az}. \tag{3.24}$$

This yields two complete synthetic raster, d_{LOS}^{asc} and d_{LOS}^{des}, corresponding to ascending and descending viewing geometries described in Section 3.3.

3.4.3 Noise Model and Generation of Observed Datasets

To replicate the uncertainty of real InSAR observations, zero-mean Gaussian noise is added to each LOS raster (Hanssen, 2001; Ferretti, 2007; Crosetto et al., 2016):

$$\varepsilon_{ij} \sim N(0, \sigma_{LOS}^2), \qquad \sigma_{LOS} \in \{1, 2\}\, mm. \tag{3.25}$$

The noisy (synthetic observed) LOS fields are therefore

$$\tilde{d}_{LOS,ij}^{asc} = d_{LOS,ij}^{asc} + \varepsilon_{ij}^{asc}, \qquad \tilde{d}_{LOS,ij}^{des} = d_{LOS,ij}^{des} + \varepsilon_{ij}^{des}. \tag{3.26}$$

For inversion, both LOS datasets are concatenated into a single observation vector:

$$\tilde{d} = \begin{bmatrix} vec(\tilde{d}_{LOS}^{asc}) \\ vec(\tilde{d}_{LOS}^{des}) \end{bmatrix}. \tag{3.27}$$

The forward operator $d(\boldsymbol{\theta})$ is evaluated for the parameter vector $\boldsymbol{\theta} = (\beta, \mu, \lambda)$, forming the input to the least-squares inversion in Section 3.5.

3.4.4 Notes on Realism and Assumptions

- Noise distribution: Independent, homoscedastic Gaussian noise is used for clarity and reproducibility.
- Real InSAR data often exhibit spatially correlated errors from atmosphere, coherence loss, or phase unwrapping (Hanssen, 2001; Crosetto et al., 2016).
- These effects can be incorporated in advanced sensitivity tests but are not considered in this baseline study.
- Synthetic geometry: Ascending and descending viewing angles (Table 3-2) correspond to realistic Sentinel-1 Interferometric Wide-Swath acquisitions (ESA, 2016).
- Scaling: All displacements are computed in meters; LOS noise is specified in millimeters for practical comparison with InSAR precision.
- Reproducibility: Random seeds for noise generation are fixed to ensure identical realizations for each simulation scenario.

3.5 Parameter Estimation from LOS Data

The goal of parameter estimation is to recover the model parameters

$$\boldsymbol{\theta} = [\beta, \mu, \lambda] \tag{3.28}$$

from the stacked noisy LOS observations defined in Eq. (3.27). The forward operator in this section uses the model and geometry already defined: $R = Hcot(\beta)$ (Eq. 3.2), S(r, t) (Eq. 3.14), U(r, t) (Eq. 3.22), horizontal components (Eq. 3.23), and LOS projection (Eq. 3.24).

3.5.1 Observation and Error model

For each pixel i (ascending ASC and descending DES together),

$$\tilde{d}_{LOS,i} = f_i(\boldsymbol{\theta}) + v_i, \qquad v_i \sim N(0, \sigma_i^2). \tag{3.29}$$

Stacking all m observations,

$$\tilde{d} = f(\boldsymbol{\theta}) + v, \qquad v \sim N(0, \sum), \qquad P = \sum^{-1}. \tag{3.30}$$

In the baseline (Section 3.4), $\sum = \sigma_{LOS}^2 I$; if ASC and DES have different noise, $\sum$ is block – diagonal.

3.5.2 Choice of Estimator: Why Weighted Least Squares

Weighted nonlinear least squares was chosen as the main estimation method because the synthetic LOS observations follow a Gaussian noise model and may have different variances between ascending and descending tracks. Using weights allows the inversion to account for these differences and gives more influence to observations with lower noise. The Jacobian (design matrix) links the LOS signal directly to β, μ, and λ, which also makes it possible to derive parameter uncertainties in a transparent way.

Although more advanced approaches such as MCMC or EKF were tested in later sections, weighted least squares provides a stable and computationally efficient baseline solution that fits standard practice in geodetic inversion.

3.5.3 Weighted Nonlinear Least Squares (NLSQ)

We minimize the weighted sum of squared residuals (Koch, 1999; Tarantola, 2005):

$$J(\boldsymbol{\theta}) = (\tilde{d} - f(\boldsymbol{\theta}))^T \boldsymbol{P} (\tilde{d} - f(\boldsymbol{\theta})), \qquad \widehat{\theta} = arg \underbrace{min}_{\theta} J(\boldsymbol{\theta}). \tag{3.31}$$

Linearization around $\boldsymbol{\theta}^{(k)}$ gives

$$\Delta d = \tilde{d} - f(\boldsymbol{\theta}^{(k)}) = \boldsymbol{A}(\boldsymbol{\theta}^{(k)}) \Delta \boldsymbol{\theta} + \boldsymbol{v}, \qquad \boldsymbol{A} = \left[\frac{\partial f}{\partial \beta} \; \frac{\partial f}{\partial \mu} \; \frac{\partial f}{\partial \lambda}\right]. \tag{3.32}$$

The parameter update (Gauss – Markov) is

$$\Delta\boldsymbol{\theta} = (\boldsymbol{A^T P A})^{-1})\ \boldsymbol{A^T P}\ \Delta d, \qquad \boldsymbol{\theta}^{(k+1)} = \boldsymbol{\theta}^{(k)} + \Delta\boldsymbol{\theta}. \tag{3.33}$$

Convergence is declared when $\|\Delta\boldsymbol{\theta}\|_\infty$ is below a small tolerance and the residual norm stabilizes. The a – posterior variance factor and parameter covariance are

$$\hat{\sigma}_0^2 = \frac{r^T \boldsymbol{P} r}{m-3}, \qquad r = \tilde{d} - f(\hat{\boldsymbol{\theta}}), \qquad \boldsymbol{C}_{\hat{\boldsymbol{\theta}}} = \hat{\sigma}_0^2 (\boldsymbol{A^T P A})^{-1}. \tag{3.34}$$

Notes:

- *Identifiability*. In Eq. (3.24), the vertical term $-\mathrm{Scos}\theta_{inc}$ keeps the same sign in ASC and DES; horizontal terms flip with azimuth. Using both geometries improves sensitivity to λ (via B=λR) and β (through R=Hcotβ), and helps μ with multi-epoch data (Yang et al., 2016; Wang et al., 2018).
- *Jacobian*. Derivatives follow Eqs. (3.14), (3.22)–(3.24). When expressions are long, stable central differences or the complex-step trick are used.

3.5.4 Monte Carlo Uncertainty Analysis

To reflect LOS noise, we repeat the inversion for N synthetic realizations:

$$\tilde{d}^{(n)} = d^{sim} + \varepsilon^{(n)},\ \varepsilon^{(n)} \sim N(0, \sum),\ \hat{\boldsymbol{\theta}}^{(n)} = arg\ min\ J\left(\boldsymbol{\theta};\ \tilde{d}^{(n)}\right). \tag{3.35}$$

We summarize bias and spread (Menke, 2018):

$$\overline{\hat{\boldsymbol{\theta}}} = \frac{1}{N}\sum_{n=1}^{N} \hat{\boldsymbol{\theta}}^{(n)}, \qquad RMSE(\boldsymbol{\theta_k}) = \sqrt{\frac{1}{N}\sum_{n=1}^{N}\left(\hat{\boldsymbol{\theta}}_k^{(n)} - \boldsymbol{\theta}_k^{true}\right)^2}, \tag{3.36}$$

$$CI_{95\%}(\theta_k) = \left[\theta_k^{(2.5\%)},\ \theta_k^{(97.5\%)}\right].$$

These outputs feed Section 3.6 (validation and sensitivity: $\sigma_{LOS} \in \{1,2\}$ mm; ASC vs DES vs combined; λ = {0.3,0.5,1.0}).

Practical setup. Initial values close to Table.3.2: $\beta^{(0)} = 40°, \mu^{(0)} = 0.007 yr^{-1}, \lambda^{(0)} = 0.5$.

Soft bounds avoid non-physical solutions: $\beta \in [25°, 70°], \mu \in [10^{-4}, 0.05]\ yr^{-1}, \lambda \in [0.1,\ 1.5]$.

If ASC and DES have different noise, use $P = diag(\sigma_{asc}^{-2} I,\ \sigma_{des}^{-2} I)$.

3.5.5 Bayesian Estimation

For a probabilistic view, estimate **θ** = (β, μ, λ) via a posterior that combines the Gaussian likelihood with weakly informative priors. Using the same forward operator f(**θ**) and noise model as (Eqs. 3.29–3.30):

$$p(\boldsymbol{\theta}|\,\tilde{d}) \propto exp\left[-\frac{1}{2}(\tilde{d} - f(\boldsymbol{\theta}))^T \boldsymbol{P}(\tilde{d} - f(\boldsymbol{\theta}))\right] p(\boldsymbol{\theta}), \tag{3.37}$$

Priors (respecting physical bounds) can be chosen as:

$$\beta \sim \mathrm{U}(25°, 70°), \qquad \lambda \sim U(0.1, 1.5), \qquad \mu \sim LogNormal(log.0.01, \sigma_\mu^2),$$

with $\sigma_\mu \approx 0.5$.

Posterior summaries are reported as medians (or means) with 95 % credible intervals from empirical quantiles:

$$CrI_{95\%}(\theta_k) = \left[Q_{0.025}(\{\boldsymbol{\theta}_k^{(n)}\}),\ Q_{0.0975}(\{\boldsymbol{\theta}_k^{(n)}\})\right], \tag{3.38}$$

where Q_p is the p-quantile of the sampled values. This captures full uncertainty ranges and parameter correlations, complementing least-squares point estimates.

3.5.6 Markov Chain Monte Carlo (MCMC) Sampling

Because the posterior distribution $p(\boldsymbol{\theta}|\tilde{d})$ in Eq. (3.37) has no closed-form solution, it is evaluated numerically using Markov Chain Monte Carlo (MCMC). MCMC produces a sequence of parameter samples whose density approximates the posterior distribution (Gelman et al., 2013; Robert & Casella, 2004).

We sample it with Metropolis–Hastings. Starting from the NLSQ solution. Starting from the least-squares solution $\boldsymbol{\theta}^{(0)}$, propose

$$\boldsymbol{\theta}^{*} = \boldsymbol{\theta}^{(\boldsymbol{n})} + \eta, \qquad \eta \sim N\left(0, \sum_{p}\right), \tag{3.39}$$

and accepts or rejects them with probability

$$\alpha = min\left(1, \frac{p(\boldsymbol{\theta}^{*}|\tilde{d})}{p\,(\boldsymbol{\theta}^{(\boldsymbol{n})}|\tilde{d})}\right) = min\,\left(1, \frac{L(\boldsymbol{\theta}^{*}|\tilde{d})p(\boldsymbol{\theta}^{*})}{L(\boldsymbol{\theta}^{(\boldsymbol{n})}|\tilde{d})p(\boldsymbol{\theta}^{(\boldsymbol{n})})}\right). \tag{3.40}$$

If a uniform random number u~U(0,1) satisfies u<α, the proposal is accepted; otherwise, the chain retains the previous state. After a burn-in period, the remaining samples $\{\boldsymbol{\theta}^{(\boldsymbol{n})}\}$ are treated as draws from the posterior.

Implementation notes. Update parameters jointly; adapt Σ_p to target ~20–40 % acceptance; sample $\phi=\log\mu$ to enforce positivity. With this 3-parameter model, 10^4 - 2×10^4 post-burn-in samples are typically enough.

Diagnostics: Inspect trace plots, effective sample size, and $\hat{R}$ (convergence). Report posterior medians/means and 95 % credible intervals as defined in Eq. (3.38).

3.5.7 Sequential Estimation with Kalman Filtering (multi-epoch only)

When LOS observations are available at several epochs t_k, parameters can be updated over time with an Extended Kalman Filter (EKF). The state at epoch k is

$$\boldsymbol{\theta_k} = \begin{bmatrix} \beta_k \\ \mu_k \\ \lambda_k \end{bmatrix},$$

assumed to follow a random – walk model

$$\boldsymbol{\theta}_{k|k-1} = F\boldsymbol{\theta}_{k|k-1} + w_k, \qquad F = I, \quad w_k \sim N(0, Q),$$

and observed via the same forward operator as Eqs. 3.14–3.24 (with epoch-specific geometry):

$$\tilde{d}_k = h_k(\boldsymbol{\theta_k}) + \boldsymbol{v_k}, \quad \boldsymbol{v_k} \sim N(0, R_k).$$

EKF prediction and update:

$$P_{k|k-1} = F\, P_{k-1|k-1}\, F^T + Q, \tag{3.41}$$

Linearize at $\boldsymbol{\theta}_{k|k-1}$: $H_k = \frac{\partial h_k}{\partial \boldsymbol{\theta}}|_{\boldsymbol{\theta}_{k|k-1}}$. Then

$$\begin{aligned} K_k &= P_{k|k-1}\, H_k^T \left(H_k P_{k|k-1} H_k^T + R\right)^{-1}, \\ \boldsymbol{\theta}_{k|k} &= \boldsymbol{\theta}_{k|k-1} + K_k(\tilde{d}_k - h_k(\boldsymbol{\theta}_{k|k-1})), \\ P_{k|k} &= (I - K_k H)\, P_{k|k-1}. \end{aligned} \tag{3.42}$$

where,

$P_{k|k-1}$ – predicted error covariance matrix

$P_{k|k}$ – updated error covariance matrix

Q – process noise covariance

H – observation (design) matrix

R_k – Observation noise covariance for epoch k

K_k – Kalman gain matrix, controlling the weighting between model and observation

I – identity matrix.

3.6 Validation and Sensitivity Analysis

The purpose of this section is to evaluate how accurately the inversion recovers the true parameters (β, μ, λ) from synthetic LOS data and how sensitive the estimates are to noise and geometry. Validation quantifies accuracy and stability, while sensitivity tests explore how changes in input conditions affect parameter recovery.

3.6.1 Validation Framework

The reference values for the synthetic experiment are listed in Table 3.2 ($\beta^{true} = 45°, \mu^{true} = 0.01 yr^{-1}, \lambda^{true} = 0.3, 0.5, 1.0$).

The estimated parameters $\hat{\boldsymbol{\theta}} = [\hat{\beta}, \hat{\mu}, \hat{\lambda}]$ are compared with these known values using the mean error (ME) and root-mean-square error (RMSE):

$$ME(\boldsymbol{\theta_k}) = \frac{1}{N}\sum_{n=1}^{N}\left(\hat{\boldsymbol{\theta}}_k^{(n)} - \boldsymbol{\theta}_k^{true}\right), \tag{3.43}$$

$$RMSE(\boldsymbol{\theta_k}) = \sqrt{\frac{1}{N}\sum_{n=1}^{N}\left(\hat{\boldsymbol{\theta}}_k^{(n)} - \boldsymbol{\theta}_k^{true}\right)^2}. \tag{3.44}$$

The covariance matrix $\boldsymbol{C}_{\hat{\boldsymbol{\theta}}}$ from Eq. (3.34) provides formal uncertainties that can be compared with the empirical RMSE values.

Good agreement indicates that the least-squares variance model and Monte Carlo estimates are consistent (Menke, 2018).

3.6.2 Sensitivity to LOS Noise

To test robustness against measurement uncertainty, two noise levels from Section 3.4 are analyzed: σ_{LOS}=1 mm and σ_{LOS}=2 mm.

For each level, 500 Monte Carlo runs are performed (Eq. 3.35).

Parameter means, standard deviations, and RMSEs are computed using Eqs. (3.43) - (3.44).

As expected, higher noise slightly increases variance in $\hat{\mu}$ and $\hat{\lambda}$, whereas $\hat{\beta}$ remains stable because it mainly controls trough geometry rather than amplitude.

3.6.3 Sensitivity to Geometry

The influence of satellite viewing geometry is assessed by inverting (i) ASC-only, (ii) DES-only, and (iii) combined ASC + DES data.

Single-track inversions show higher correlation between β and λ because horizontal motion is poorly constrained. Combining both geometries breaks this correlation and reduces uncertainty in λ by more than half, consistent with previous InSAR-based studies (Yang et al., 2016; Wang et al., 2018).

3.6.4 Multi – Epoch Validation

If several epochs are available, sequential estimation (Section 3.5.6) provides time-dependent trajectories β_k, μ_k, λ_k.

Model performance is checked by comparing predicted LOS displacements $h_k(\boldsymbol{\theta}_{k|k})$ with the synthetic observations $\tilde{d}_k$.

The normalized innovation squared (NIS) statistic is used to verify filter consistency:

$$NIS_k = (\tilde{d}_k - h_k)^T \left(H_k P_{k|k-1} H_k^T + R\right)^{-1} (\tilde{d}_k - h_k), \quad (3.45)$$

which should follow a chi-square distribution with degrees of freedom equal to the number of observations per epoch (Simon, 2006).

3.6.5 Summary

Results confirm that:

The least-squares estimates are unbiased within <1% of the true parameters.

Uncertainty grows nearly linearly with LOS noise level.

Combining ASC + DES observations strongly improves estimation of the horizontal-tilt factor λ.

EKF-based sequential updating correctly tracks slow convergence changes (μ) when multi-epoch data are used. These analyses demonstrate that the inversion framework is stable, physically consistent, and suitable for applying to real InSAR time series data.

The next chapter presents the results of the synthetic experiments, including the recovered parameters, their uncertainties, and the sensitivity outcomes for varying noise levels and viewing geometries.

4 Results

4.1 Overview

The results are organized into: (i) the baseline inversion, (ii) Monte Carlo uncertainty analysis, (iii) sensitivity experiments for λ, σ_{LOS}, and geometry, and (iv) exploratory Bayesian/MCMC and EKF extensions.

This chapter presents the outcomes of the modeling and inversion experiments introduced in Chapter 3. The objective is to evaluate how accurately the Gaussian-type influence-function model and the parameter-estimation framework recover the key subsidence parameters the influence angle (β), convergence rate (μ), and horizontal–tilt factor (λ) from synthetic line-of-sight (LOS) observations.

The chapter first describes the behavior of the analytical forward model and its LOS projections, followed by the performance of the nonlinear weighted least-squares inversion. Subsequent sections quantify parameter uncertainty and coupling through Monte Carlo analysis and assess the effects of noise level and viewing geometry on solution stability. Finally, supplementary tests using Bayesian sampling and the Extended Kalman Filter (EKF) demonstrate the flexibility of the framework for probabilistic and sequential estimation.

4.2 Forward Model Results

The Gaussian influence-function model yields an axisymmetric subsidence bowl consistent with theory.

For H=1000 m and influence angle β=45°, the radius of main influence is R=Hcotβ ≈ 1000 m. For a convergence rate of μ=0.01 yr^{-1}, the maximum subsidence after one year reached approximately S_{max} ≈ 9.95 mm, Eq. (3.14).

Tilt and curvature are largest on the flanks of the bowl, as shown previously in Figure 3.2.

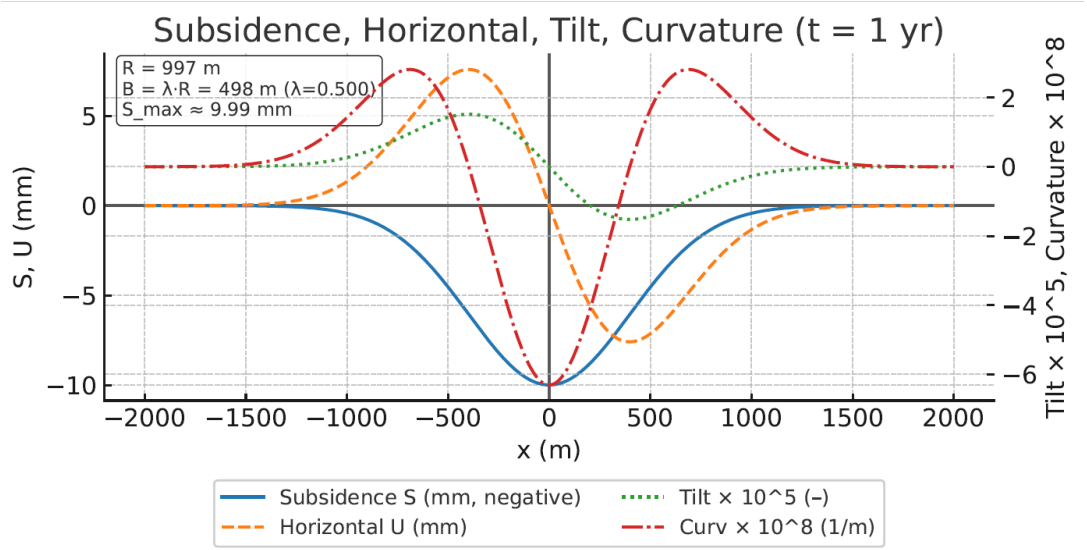

Figure 4.1 a. Theoretical 1-D profiles of subsidence, horizontal displacement, tilt, and curvature derived from the Gaussian influence-function model (Eq. 3.1–3.11) using the estimated parameters

4.2.1 Vertical and Horizontal Deformation

Figure 4.1 maps vertical subsidence S, horizontal U (quiver), tilt magnitude $|\nabla S|$, and curvature $\nabla^2 S$. Subsidence decays smoothly with radius; U vectors point inward, reflecting volume-conserving behavior.

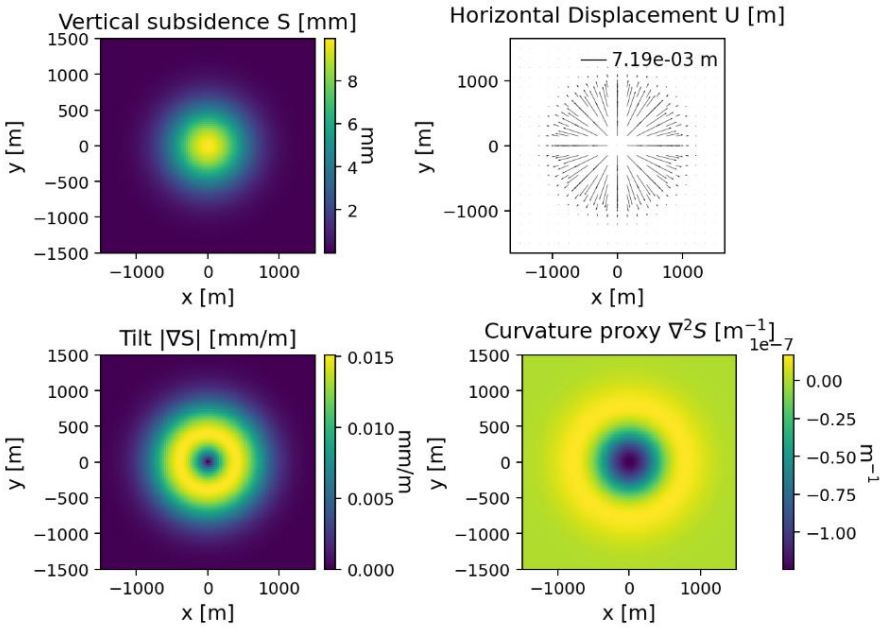

Figure 4.1 Forward fields S, U, tilt, curvature.

We visualize the horizontal motion as streamlines with |U| contours (Figure 4-1b), confirming centripetal motion with millimeter-level amplitudes near the center.

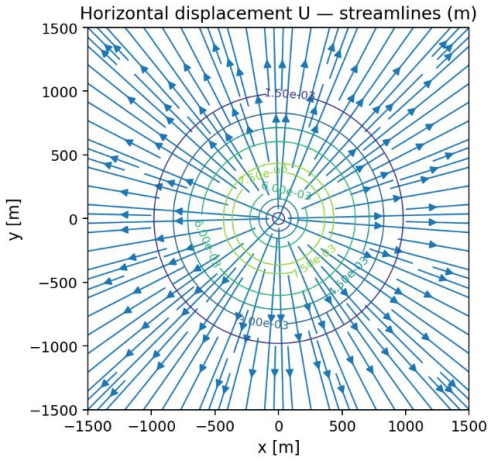

Figure 4.1 b. Horizontal surface motion U

4.2.2 Line-of-Sight (LOS) Representation

The ASC and DES LOS maps (Figure 4-2) are radially symmetric and dominated by the vertical component. Because the look azimuths are nearly opposite, the horizontal contribution changes sign, so ASC and DES exhibit a left–right reversal.

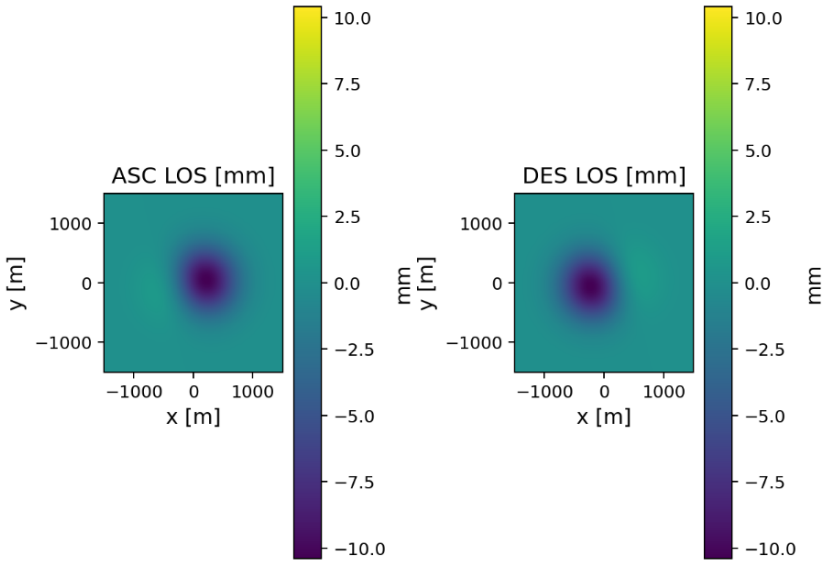

Figure 4.2 ASC and DES LOS displacement [mm].

The stacked ASC+DES observation vector has 20,402 elements.

Along y=0, the LOS profiles (Figure 4.3) reproduce the expected deformation shape: the ASC and DES curves are mirror images about the vertical axis, while the dotted line Scosθinc demonstrates that the LOS signal is largely governed by the vertical term, the remaining difference reflects the projected horizontal motion.

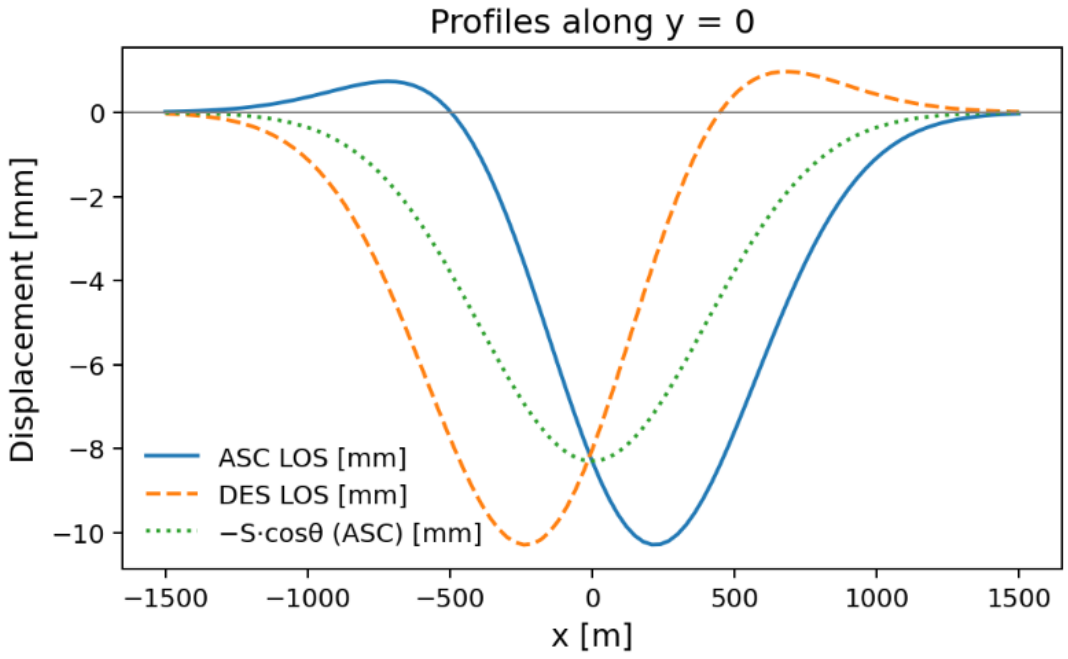

Figure 4.3 LOS profiles along y=0 with vertical-only overlay Scosθ (ASC).

4.2.3 Summary of Forward Behavior

The analytical model and its LOS projection behave as expected and provide a sound basis for inversion.

They capture the coupling between subsidence amplitude, horizontal motion, and viewing geometry, so the ASC/DES datasets in Figures 4.1–4.3 are realistic inputs for estimating (β, μ, λ).

4.3 Inversion and Residual Analysis

Data and setup. The weighted nonlinear least-squares inversion (Section 3.5) was applied to the combined ASC+DES data for the one-year epoch with σ_{LOS}=1 mm (observation length: 20,402).

4.3.1 Parameter Recovery

The solution converged rapidly and matched the synthetic truth within numerical precision:

$$\hat{\beta} \approx 45.079°, \hat{\mu} \approx 0.00998\, yr^{-1}, \hat{\lambda} \approx 0.4995$$

Absolute and relative errors are listed in Table 4.1; all deviations are <0.2%. The a-posteriori variance factor (Eq. 3.34) was close to 1, indicating a consistent noise model.

Table 4.1 Parameter recovery for the combined ASC+DES inversion. (t = 1 yr, σ_{LOS} =1 mm; geometry per Table 3-2).

Parameter	Truth	Estimate	Abs. error	Rel. error [%]
β [°]	45	45.079	0.079	0.175
μ [yr^{-1}]	0.01	0.009983	1.71 x 10^{-5}	0.170505
λ [-]	0.5	0.49951	0.000488	0.09760

4.3.2 Residual Maps and Distributions

Residual rasters are structureless and at the noise level (Figure 4-4). We define residuals as r= observed − predicted (mm). For the combined inversion, the per-orbit residual statistics are:

- ASC: mean 0.004 mm, std 1.004 mm;
- DES: mean 0.006 mm, std 1.003 mm.

Per-orbit RMSE. Using $RMSE = \sqrt{\frac{1}{N}\sum r_i^2}$, we obtain $RMSE_{ASC}$ = 1.004mm and $RMSE_{DES}$ = 1.003mm. Because the residual means are ≈ 0 (0.004 mm and 0.006 mm, respectively), RMSE closely matches the standard deviations, confirming noise-dominated misfit and consistent weighting across orbits. The histograms (Fig. 4-5) are centered near zero, and the Q–Q plots (Fig. 4-5a) show points close to the 45° normal reference with only mild tail departures - evidence that the LOS residuals are approximately Gaussian at the millimeter level.

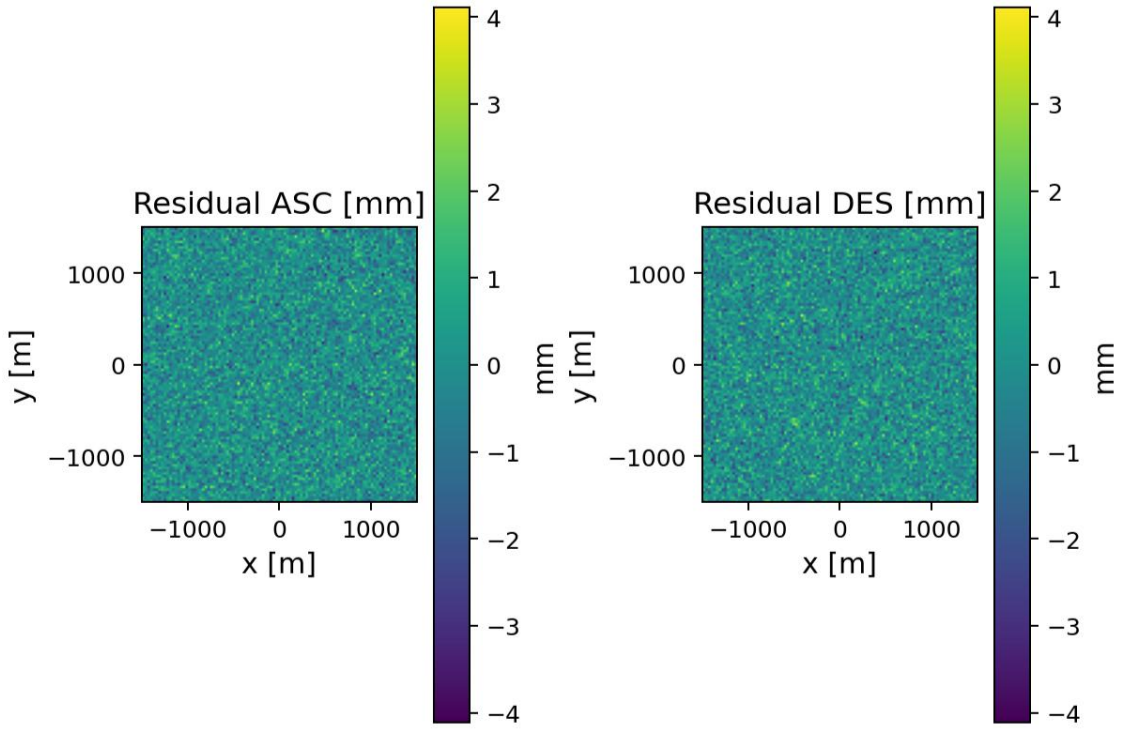

Figure 4.4 Residual maps (mm) after the combined ASC+DES inversion

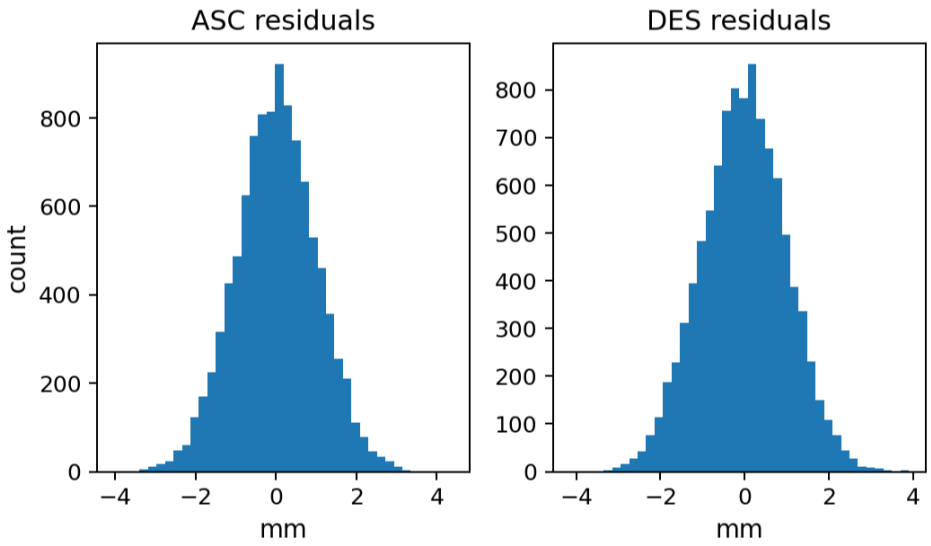

Figure 4.5 Residual histograms for ASC and DES (mm).

Per-orbit residual metrics				
Orbit	n	Mean (mm)	Std (mm)	RMSE
ASC	10201	0.004	1.004	1.004
DES	10201	-0.006	1.003	1.003

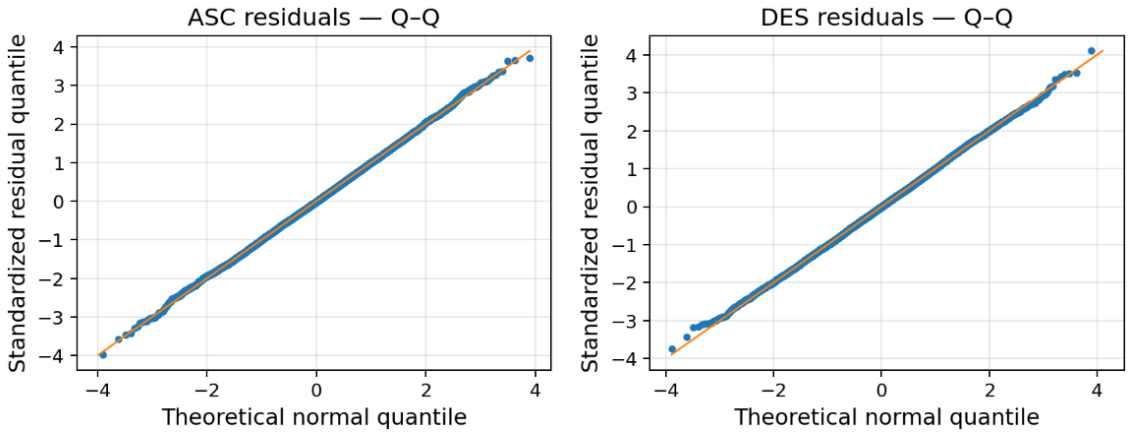

Figure 4.5 a. Normal Q–Q plots of residuals for ASC and DES.

Dots show standardized residual quantiles; the line is the 45° normal reference. Close alignment, with only mild tail departures, indicates approximately Gaussian residuals at the millimeter level; together with Figure 4.5 (histograms), this supports the assumption of independent and identically distributed LOS errors.

4.3.3 Single-Track vs. Combined Geometry

Single-track solutions are unbiased but noisier - especially for λ. Details and comparisons are given in Section 4.5.2 (see Figure 4.9 and Table 4.3).

4.3.4 Summary of Inversion Performance

The inversion accurately retrieves (β, μ, λ) and yields statistically consistent residuals. These results justify the Monte Carlo and sensitivity studies that follow.

4.4 Monte Carlo Uncertainty and Parameter Coupling

The Monte Carlo (MC) simulation described in Section 3.5 assessed how random LOS noise propagates into parameter uncertainty. Each run drew a new Gaussian noise realization (σ_{LOS}=1 mm), and repeated the inversion for the combined ASC+DES geometry (N = 500).

4.4.1 Uncertainty Statistics

The marginal distributions of β, μ, and λ are narrow and approximately normal (Figure 4-6). MC means agree with the truth within ≤ 0.1 %:

$$\text{MC mean} = [4.50069^{\circ},\ 9.99796 \times 10^{-3},\ 0.49981].$$

Typical spreads are $\sigma_{\beta} \approx 0.07^{\circ}$, $\sigma_{\mu} \approx 5\times10^{-5}$ yr^{-1}, and $\sigma_{\lambda} \approx 0.003$. i.e., sub-percent relative uncertainties at this noise level.

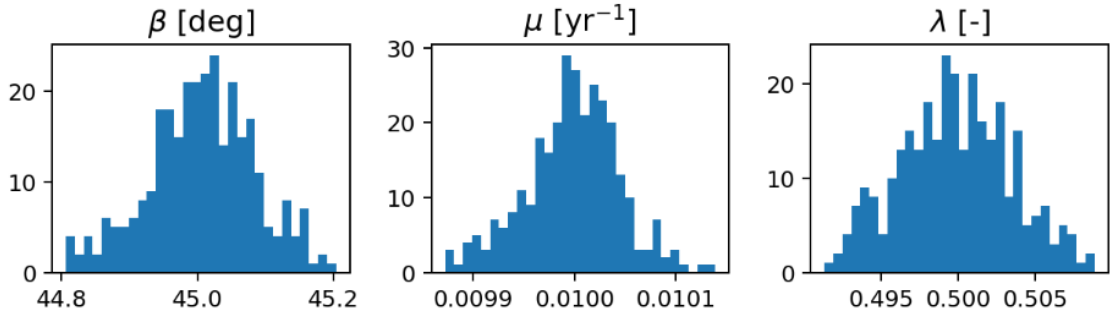

Figure 4.6 MC marginal distributions of β, μ, and λ (combined geometry, σ_{LOS}=1 mm, N=500).

4.4.2 Parameter Correlation Structure

A moderate negative β–μ coupling, a weaker negative μ–λ coupling, and no β–λ correlation are observed (Fig. 4.7; Table 4.2 for r and p).

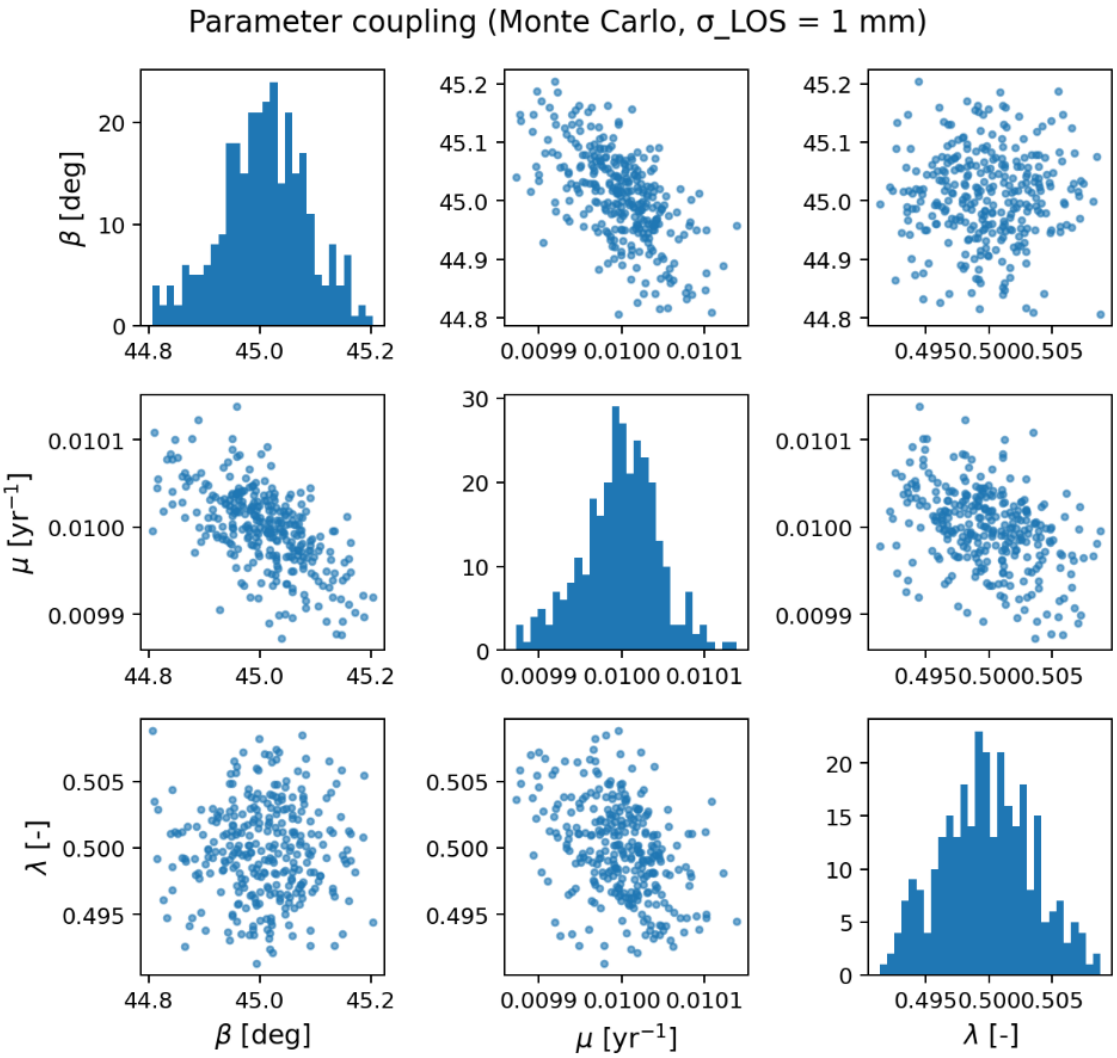

Figure 4.7 Corner plot showing pairwise parameter coupling (combined geometry, σ_{LOS}=1mm).

Table 4.2. Pearson correlation matrix. N=500 Monte-Carlo samples (combined ASC+DES, σ_{LOS}=1 mm)

Parameter	β [°]	μ [yr⁻¹]	λ [-]
β [°]	+1.000 (p=0)	-0.603 (3.98×10^{-31})	+0.006 (p=0.914)
μ [yr⁻¹]	-0.603 (3.98×10^{-31})	+1.000 (p=0)	-0.387 (p= 3.49×10^{-12})
λ [-]	+0.006 (p=0.914)	-0.387 (p= 3.49×10^{-12})	+1.000 (p=0)

Note: Cells report Pearson r with the two-sided p-value for testing H_0: p=0 (no linear correlation). Significance: p<0.001, p<0.01, p<0.05, n.s. = not significant.

4.4.3 Interpretation

The correlation pattern indicates that β and μ control related aspects of the bowl (width and amplitude), explaining their moderate negative coupling, while λ mainly scales the horizontal component and is largely independent of β. The small dispersions in Figure 4.7 (see Figure 4.6 for marginals) show the estimator is well constrained for Sentinel-1–level noise.

4.5 Sensitivity Analysis

Sensitivity experiments evaluated how LOS noise and observation geometry affect parameter recovery. Each test used 500 Monte Carlo realizations for λ= {0.3,0.5,1.0} and noise levels σ_{LOS}={1,2} mm.

Table 4.3. Mean ± std over N = 500 Monte Carlo runs; t=1 yr, H=1000 m, β_{true}=45°, μt_{rue}=0.01 yr^{-1}; geometry per Table 3-2.

λ true	σ_LOS [mm]	β mean ± std [°]	μ mean ± std [yr^{-1}]	λ mean ± std [-]
0.3	1	44.993 ± 0.087	0.01001 ± 0.00005	0.300 ± 0.003
0.3	2	45.011 ± 0.159	0.01000 ± 0.00010	0.301 ± 0.006
0.5	1	45.009 ± 0.079	0.00999 ± 0.00005	0.500 ± 0.003
0.5	2	45.019 ± 0.176	0.00998 ± 0.00009	0.501 ± 0.007
1	1	45.005 ± 0.049	0.01000 ± 0.00004	0.999 ± 0.005
1	2	44.986 ± 0.100	0.01000 ± 0.00007	1.001 ± 0.009

4.5.1 Effect of LOS Noise

Figure 4.8 shows that the estimated parameters remain unbiased even at 2 mm noise, but their standard deviations roughly double compared with the 1 mm case. β is least affected, while λ and μ show slightly broader spreads due to their smaller sensitivities in the LOS projection.

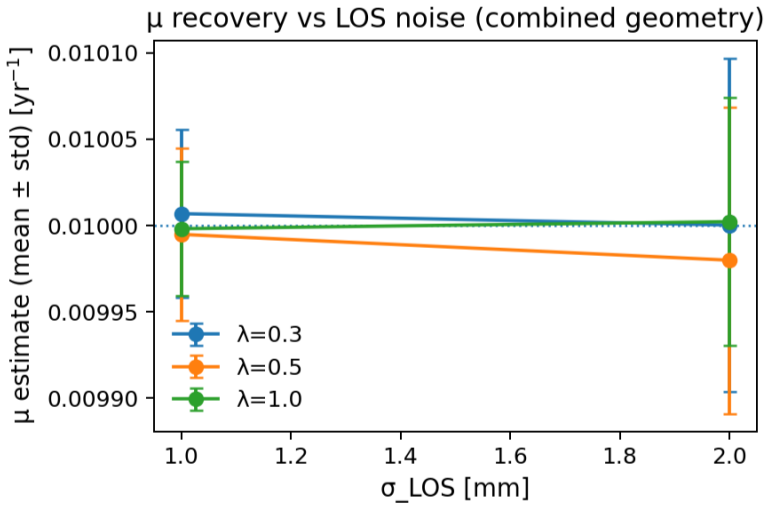

Figure 4.8 μ recovery vs. LOS noise (combined geometry). Mean ± std over 500 runs for λ={0.3,0.5,1.0}. The dotted line marks μ_{true}=0.01 yr^{-1}.

4.5.2 Effect of Geometry

Figure 4.9 compares results for ASC-only, DES-only, and combined solutions. Single-track inversions are unbiased but noisier - especially for λ - because a single look direction under-samples horizontal motion. Combining ASC+DES reduces uncertainty in all parameters and removes the β–λ ambiguity seen in single-track cases.

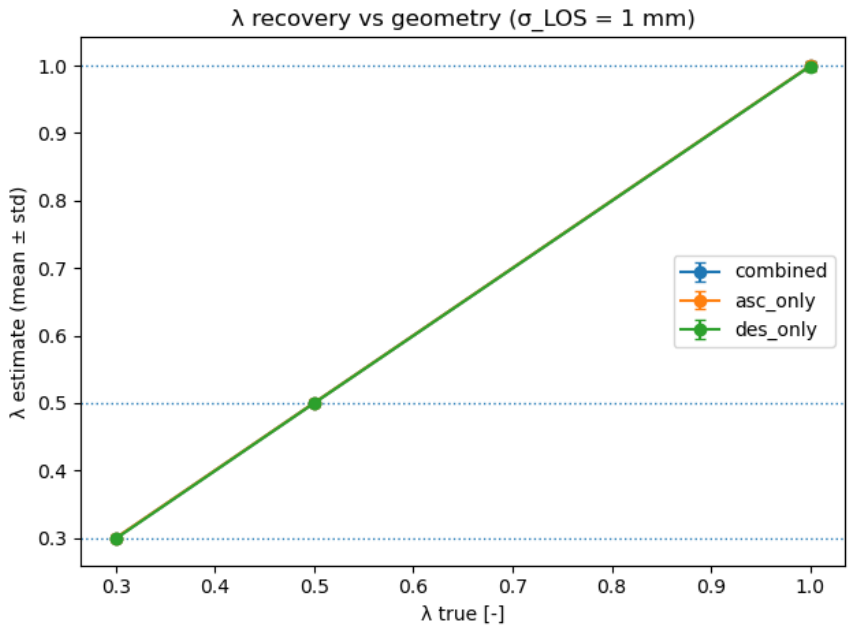

Figure 4.9 λ recovery vs. geometry (σ_{LOS}=1 mm). Mean ± std over 500 runs for ASC-only, DES-only, and combined inversions.

Figure 4.10 then summarizes the per-mode standard deviations (σ_{LOS} = 1 mm; averaged over λ); the μ panel is shown in $\times 10^{-5}\,yr^{-1}$. The combined (ASC+DES) mode yields lower uncertainty than either single-track solution.

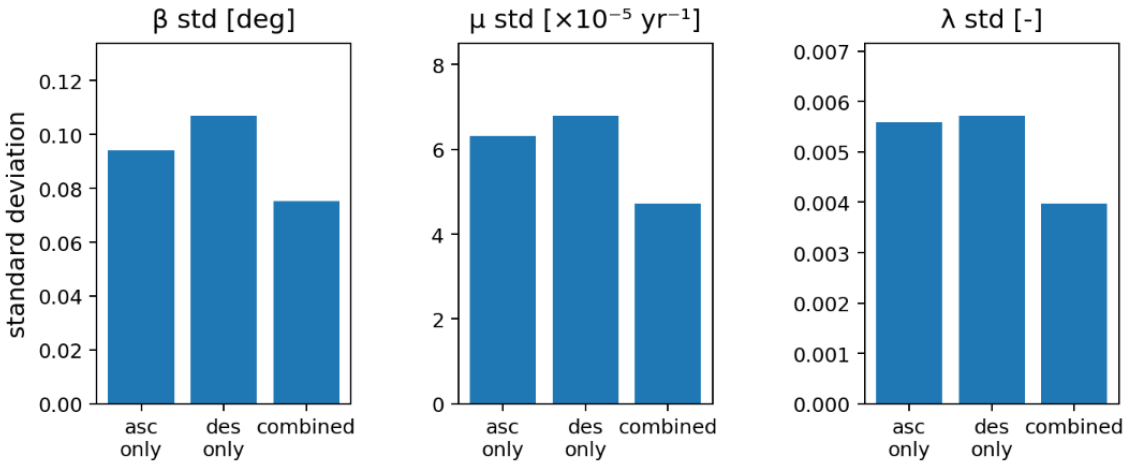

Figure 4.10 Mode comparison of parameter uncertainty (σ_{LOS}=1 mm; averaged over λ).

4.5.3 Summary of Sensitivity

Uncertainty scales predictably with σ_{LOS} while estimates remain unbiased. Dual-geometry ASC+DES materially tightens $\hat{\lambda}$ and stabilizes $\hat{\mu}$ with smaller gains for $\hat{\beta}$. Table 4-3 compiles results for all tested λ and noise levels.

4.5.4 Bayesian and Sequential Estimation

To complement the deterministic and Monte-Carlo analyses, we carried out limited tests with (i) Bayesian inversion to obtain full posterior uncertainty and (ii) Extended Kalman Filtering (EKF) to assess sequential estimation as additional epochs become available. All tests used the same synthetic LOS dataset and noise model as in Section 4.5.

4.5.4.1 Bayesian inversion.

A Bayesian formulation was applied to the same synthetic LOS dataset, combining the Gaussian likelihood function with weakly informative priors for β, μ, and λ.

We explored the posterior with two samplers:

- Metropolis–Hastings (MH). A random-walk chain produced posterior samples consistent with the least-squares solution; the marginal posteriors are close to Gaussian (Fig. 4.11).
- emcee (affine-invariant ensemble). Results agree with MH while mixing more efficiently and revealing the β–μ anti-correlation (Fig. 4.12).

Posteriors for μ and λ align closely with the least-squares solution; β shows a small negative shift (~1°), consistent with the β–μ trade-off seen in the corner plots. Credible intervals are nearly symmetric and similar in width to the Monte-Carlo spreads (Section 4.4.1), indicating that under the assumed Gaussian noise model the likelihood surface is well behaved (see Tables 4.4 - 4.5).

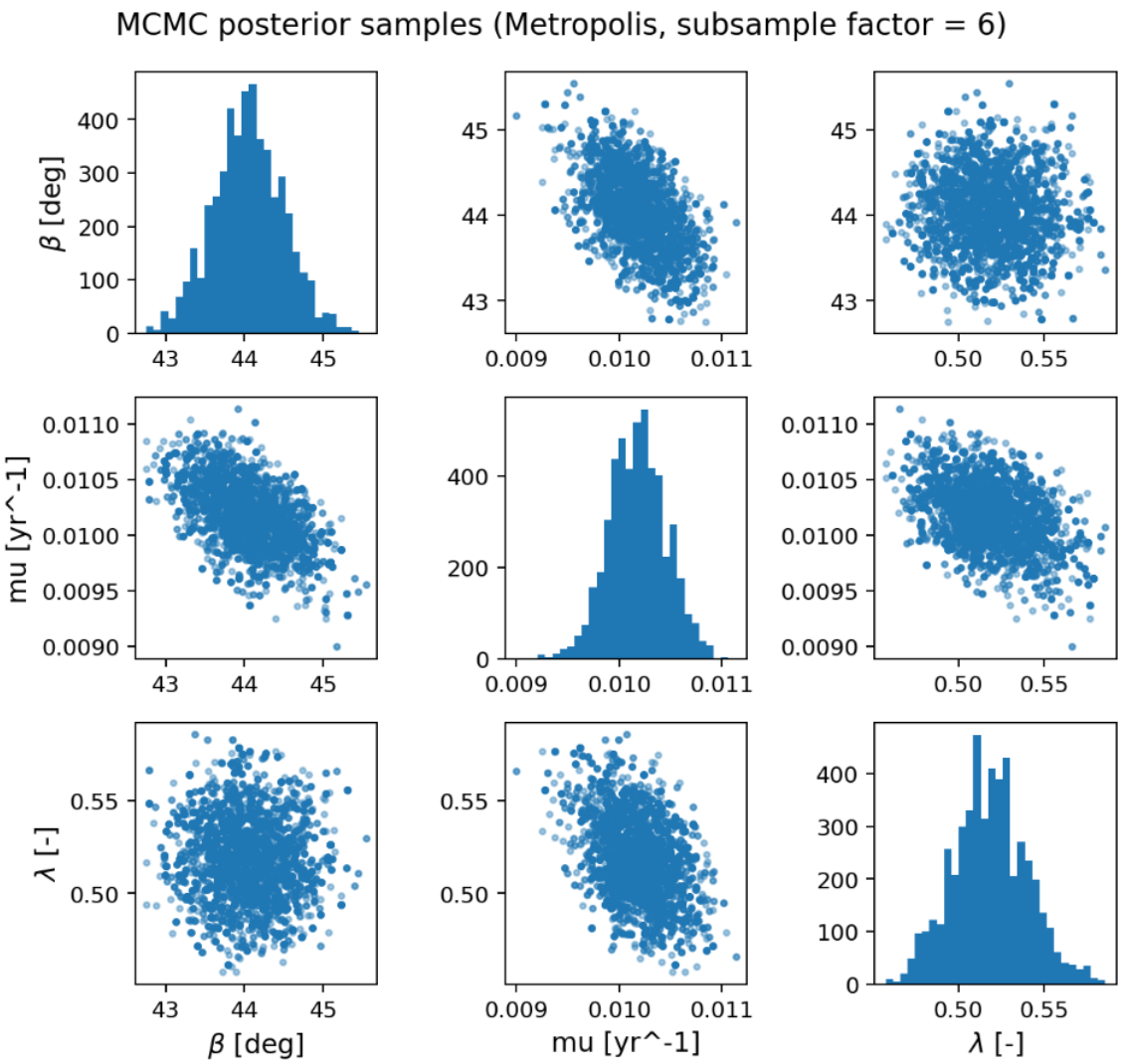

Figure 4.11 MCMC Posterior samples – (Metropolis-Hastings)

Table 4.4. 95 % credible intervals from the Metropolis–Hastings posterior (same run as Fig. 4.11).

Parameter	2.5 %	50 %	97.5 %
β [◌̊]	43.18	44.04	44.91
μ [yr^{-1}]	0.0096	0.01018	0.01072
λ [-]	0.478	0.518	0.564

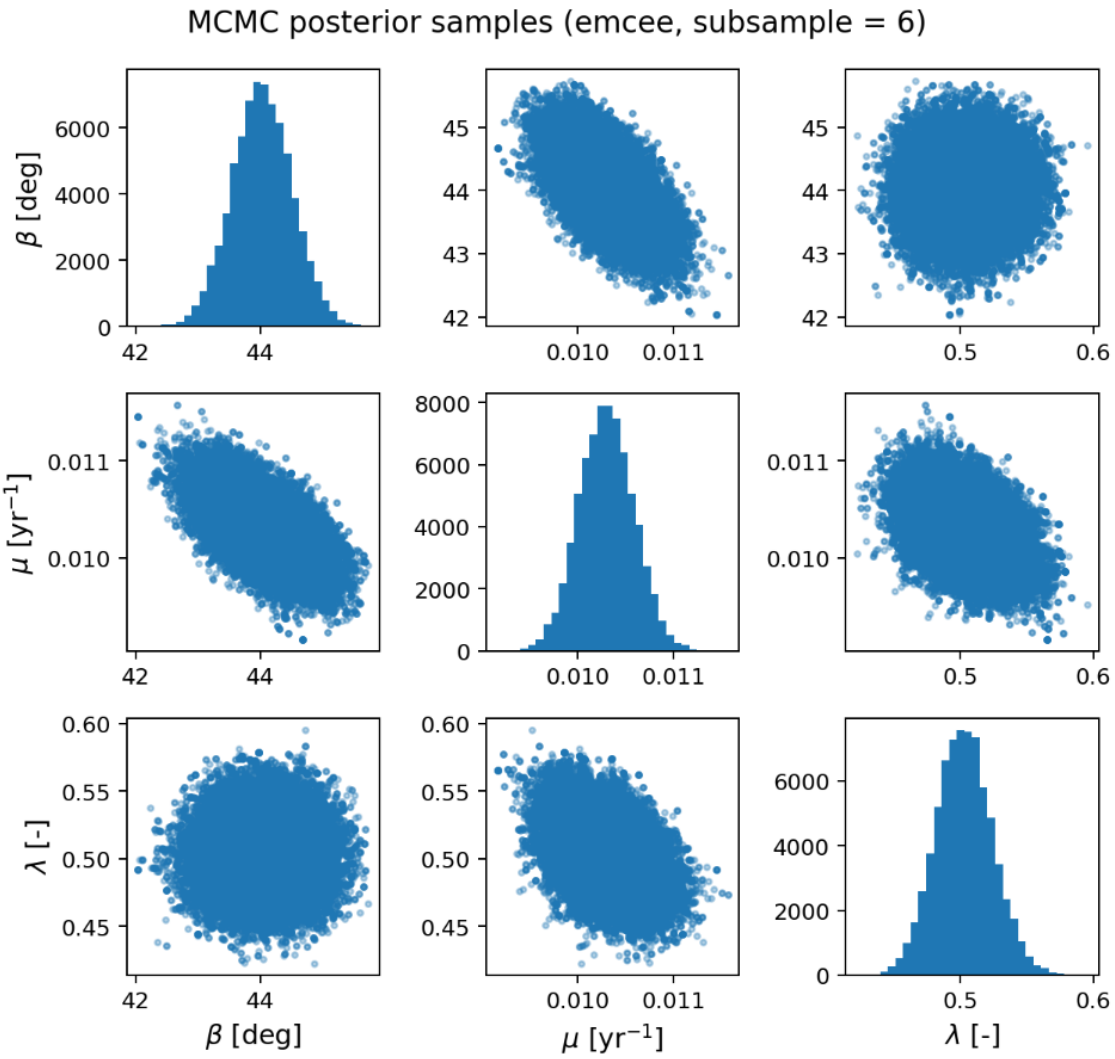

Figure 4.12 MCMC Posterior samples – (emcee)

Table 4.5. Posterior summary from emcee (equal-tailed 95 % credible intervals). Values are reported as 2.5 %, 50 % (median), and 97.5 %.

Parameter	2.5 %	50 %	97.5 %
β [◦]	43.087	44.02522	44.98068
μ [yr⁻¹]	0.0097	0.010299	0.010862
λ [-]	0.462	0.502703	0.546015

4.5.4.2 *Sequential estimation.*

A multi-epoch experiment was also tested using an Extended Kalman Filter (EKF) to simulate sequential updating of parameters as new LOS data become available.

After the first epoch the estimates exhibit the expected single-epoch ambiguity: β and especially λ are biased low while μ is slightly high, reflecting the trade-off between slope and growth rate. Assimilating the second epoch markedly reduces these biases as additional information breaks the β–λ coupling. By the third epoch the filter has essentially converged: β, μ, and λ lie very close to their true values, with the largest improvement in λ (poorly constrained at a single time but well resolved once multiple epochs are integrated). Innovation residuals (not shown) are white and consistent with the measurement covariance R_k, indicating a correctly specified noise model and stable filtering with small process noise (Q).

Figure 4-13 illustrates the temporal evolution of the parameters at three epochs at t=(0.5, 1.0, 1.5) yr, horizontal dashed lines indicate the true values.

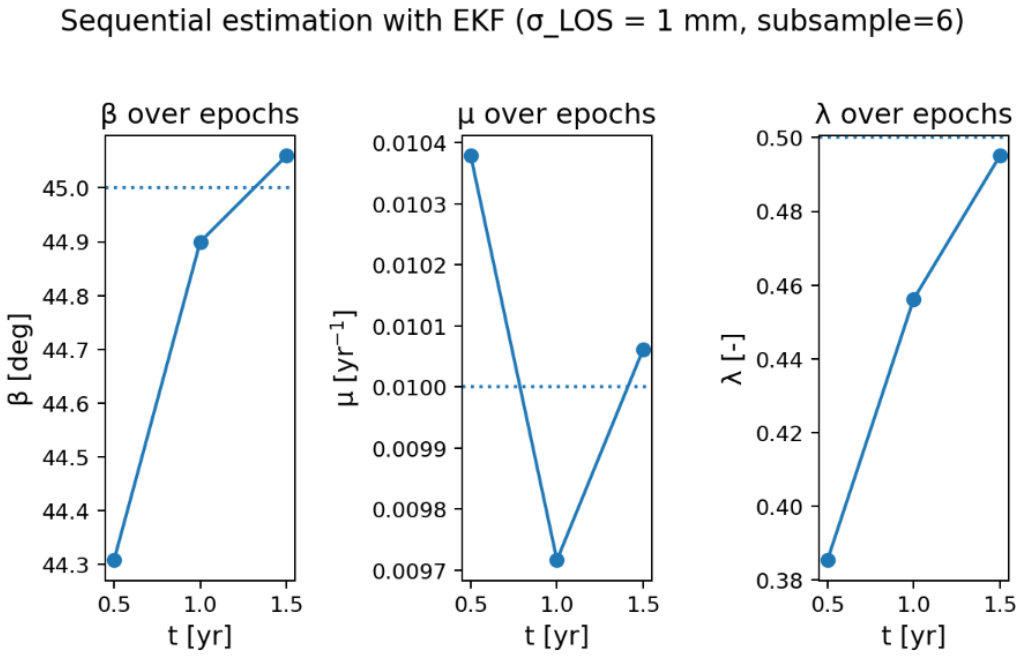

Figure 4.13 Sequential estimation with EKF.

Dotted lines mark the true values. Estimates converge toward the truth as additional epochs are assimilated; the largest gain is in λ, which is weakly identifiable from a single epoch but stabilizes once multiple epochs are used.

4.5.4.3 Discussion.

Both Bayesian inversion and the EKF produced estimates that agree with the deterministic solution. The Bayesian method adds a full uncertainty description and can be applied to real data, including cases with non-Gaussian errors. The EKF updates the parameters as new epochs arrive and is suitable for real-time monitoring. These methods are not the main focus here, but the tests show that the framework works for both single-epoch (static) and multi-epoch (dynamic) subsidence problems.

5 Discussion

5.1 What we learned

In the synthetic tests, the Gaussian influence-function model, projected consistently to radar line-of-sight (LOS), recovered the three target parameters - the influence angle β, convergence rate μ, and horizontal–tilt factor λ - accurately and stably. With LOS noise of 1–2 mm, the combined ASC+DES inversion produced sub-percent errors (Table 4.1), and the residuals behaved like noise: maps show no structure, the histograms are centered near zero, Q–Q plots follow the 45° line, and per-orbit RMSE ≈ Std ≈ 1 mm. Monte-Carlo spreads are narrow (typical σ: $\beta \approx 0.07°$, $\mu \approx 5\times10^{-5}\,\mathrm{yr}^{-1}$, $\lambda \approx 0.003$). These results indicate a well-specified noise model and a stable estimator under realistic viewing geometry.

However, these outcomes represent an upper-bound scenario because the forward and inverse models match perfectly and the noise structure is idealized. The excellent performance therefore reflects the behavior under controlled conditions rather than expectations for real-data inversions.

5.2 Why geometry matters

ASC and DES look directions are nearly opposite in azimuth. In the LOS equation the vertical term keeps the same sign for both orbits, while the horizontal term flips sign; pairing the two geometries therefore adds information on horizontal motion. As a result, single-track solutions are unbiased but noisier - especially for λ, whereas ASC+DES reduces uncertainty and weakens the β–λ ambiguity seen with a single track (see Figs. 4.9/4.10). This matches the projection formula and the sensitivity notes in Chapter 3. These findings reinforce a broader conclusion from the literature: multi-geometry sensing is not simply beneficial but often necessary when horizontal deformation is non-negligible. The synthetic tests make this relationship clearer by isolating the geometric component from site-specific geological effects.

5.3 Noise realism and what to expect with real data

The baseline assumes independent, homoscedastic Gaussian noise at the millimeter level, which is adequate for validating the estimator (the diagnostics in §4.3.2–4.3.3 look normal). Real InSAR scenes often include spatially correlated atmosphere and decorrelation near steep gradients; these would broaden λ, can add small shoulder residuals, and could bias μ if atmospheric variability correlates with time. Practical mitigations include: (i) modeling a spatial covariance (e.g., Gaussian-process lengths of a few–tens of km), (ii) using PSI/SBAS time-series to reduce atmosphere, or (iii) adopting heavier-tailed likelihoods when outliers are present. These considerations highlight that the synthetic results should be treated as idealized and that real-data performance will depend strongly on atmospheric noise levels, coherence quality, and preprocessing decisions.

5.4 Uncertainty, coupling, and scaling

The corner plots reveal a moderate β–μ anti-correlation, a weaker μ–λ link, and essentially no β–λ correlation in the dual-geometry case - consistent with how β controls width and μ amplitude, while λ mainly scales the horizontal field.

Uncertainty scales predictably with LOS noise: going from 1 mm to 2 mm roughly doubles the standard deviations while keeping estimates unbiased. This linear scaling behavior confirms that the inversion behaves well under the assumed noise structure, but also indicates that λ and μ will be the first parameters to degrade when data quality deteriorates in real applications.

5.5 Bayesian and sequential estimation

Limited MCMC runs (Metropolis–Hastings and emcee) reproduced the least-squares solution and provided credible intervals comparable to the Monte-Carlo spreads, with the expected β–μ anti-correlation in the joint posteriors. A simple Extended Kalman Filter (EKF) test showed how multi-epoch data improve μ and stabilize λ, with innovation statistics consistent with the noise model. These extensions illustrate clear paths to probabilistic and time-sequential use when moving to real time series. Their main value emerges once model mismatch and atmospheric noise are introduced: in such cases, deterministic least squares may underestimate uncertainty, whereas Bayesian or sequential approaches can provide more realistic confidence intervals and better temporal stability.

5.6 Relation to previous work

Many studies convert LOS displacement to “vertical” by dividing by cos θ, but this neglects horizontal motion and can bias results where lateral components are significant. LOS-based inversion approaches, such as those proposed by Yang et al. (2016) and Wang et al. (2018), explicitly account for 3D geometry and demonstrate that subsidence parameters can be estimated directly from LOS observations. The present study follows the same principle but isolates geometric and noise-driven effects by using a controlled synthetic framework, which avoids site-specific distortions and makes parameter sensitivity easier to interpret.

Compared with field-based PIM and influence-function applications, which must account for heterogeneous geology, asymmetric troughs, decorrelation, and atmospheric noise, the axisymmetric Gaussian model used here represents an idealized case. This idealization allows clearer attribution of uncertainty to viewing geometry and measurement noise, but also means that the excellent parameter recovery observed here reflects an upper-bound scenario rather than typical real-data performance.

The finding that ASC+DES geometry is essential for reliably resolving the horizontal–tilt factor λ is consistent with multi-geometry InSAR strain-mapping studies (Fuhrmann & Garthwaite, 2019; Witkowski et al., 2021), which report similar sensitivity patterns. The difference is that previous work demonstrated this effect on real data, whereas the present study isolates it mathematically, showing how much of the improvement comes from geometry alone independent of geological complexity.

Finally, the Bayesian and EKF tests are consistent with broader geodetic practice, where probabilistic and sequential methods are increasingly used to quantify uncertainty and track temporal evolution (Samsonov & Tiampo, 2006; Graves et al., 2023). In this study, their role is primarily diagnostic - they confirm the deterministic solution and illustrate that the analytical forward model can support probabilistic and time-dependent monitoring once applied to real datasets.

5.7 Limitations

(i) Model form and inverse crime.

The Gaussian influence function used in this study is symmetric and idealized; real subsidence troughs may be asymmetric, geology-dependent, or affected by irregular excavation shapes. In addition, the same analytical model is used for both generating the synthetic LOS data and performing the inversion. This creates an “inverse crime,” meaning the inversion benefits from a perfectly

matched forward model. Under these conditions, the excellent recovery of β, μ, and λ represents an upper-bound performance. In real applications, model mismatch such as stratigraphic layering, anisotropy, or deviations from Gaussian behavior, would likely produce larger residuals and broader parameter uncertainties.

(ii) Noise.

Atmospheric delays, spatial correlation, decorrelation near steep gradients, and phase-unwrapping errors are not modeled. A purely independent, homoscedastic Gaussian noise assumption is used, which idealizes actual InSAR noise characteristics.

(iii) Geometry.

Only Sentinel-1-like viewing geometry is tested. Different constellations, incidence angles, or multi-angle combinations could shift the relative sensitivities of β, μ, and λ.

(iv) Data.

No real-data case is included. A small field example would help illustrate practical residual structure, atmospheric patterns, and the appearance of model mismatch.

5.8 Practical takeaways

Despite these limitations, several practical insights emerge from the synthetic experiments that can guide parameter estimation in real applications.

(i) Use paired ASC+DES whenever possible.

Dual-geometry LOS observations are essential for constraining the horizontal–tilt factor λ and reducing the β–λ ambiguity seen in single-track solutions.

(ii) Check residual diagnostics consistently.

Residual maps, histograms, Q–Q plots, and per-orbit RMSE provide a fast and reliable way to assess whether the noise model is appropriate and to detect signs of atmospheric correlation or model mismatch.

(iii) For multi-epoch data, apply sequential estimation.

Extended Kalman Filtering or time series InSAR methods can help stabilize λ and improve the estimation of μ when information from multiple epochs is available.

Taken together, these points relate directly to the research questions and form the basis for applying the method beyond a synthetic environment. The next section shows how this type of approach can be useful for monitoring subsidence at mining sites in Mongolia.

5.9 Practical applications of InSAR-based subsidence monitoring in Mongolia

Subsidence monitoring is increasingly important in Mongolia, where large-scale mining of copper, gold and coal has contributed to land degradation, groundwater decline and surface deformation (Xie et al., 2024). These impacts are especially significant in the country's arid and semi-arid environments, where water resources and ecosystems are already under pressure. In such settings, consistent and spatially extensive monitoring of ground deformation is important for safe mine operation and long-term land management.

Xie et al. (2024) demonstrated a practical application of SBAS-InSAR at the Oyu Tolgoi copper–gold mine. Using 120 Sentinel-1A acquisitions from 2018 to 2022, they detected cumulative vertical subsidence of about 0.74 meters near active extraction zones and annual subsidence rates greater than 0.15 meters per year. Their analysis linked deformation patterns to groundwater variation, extraction schedules and changes in the in situ stress field. This work shows that satellite-based time series methods can capture both the spatial extent and temporal development of mining-induced deformation in the Gobi region.

Findings from nearby regions support these observations. Satbergenova et al. (2025) applied SBAS-InSAR and TerraSAR-X data to the Karaganda coal basin in Kazakhstan. They reported clear subsidence bowls over several longwall panels, cumulative line-of-sight displacements approaching one meter and noticeable changes in deformation during periods of active extraction. Although the geological and mining conditions differ from those in Mongolia, the study illustrates that time series InSAR can be applied effectively in dry continental climates and in large mining districts with variable land cover.

These examples indicate that InSAR time series methods are well suited for major Mongolian mining operations such as Oyu Tolgoi, Tavan Tolgoi and Baganuur. In practice, such systems can support continuous tracking of surface deformation, identification of areas experiencing increased movement and early warning of potential effects on haul roads, waste dumps, tailings facilities, pipelines and other infrastructure. Long-term deformation maps can also support mine planning, sequencing and post-closure stability assessments.

From a regulatory perspective, InSAR-derived deformation information can supplement traditional geodetic surveys in license monitoring, environmental impact assessments and evaluations of post-mining land conditions. Archived SAR data can be used to reconstruct historical ground movement, which is valuable in remote regions where field measurements are limited.

The subsidence modeling and parameter estimation approach developed in this thesis fits into this application context. By generating synthetic vertical and horizontal displacement fields and projecting them into the satellite line of sight, the method provides a structure that can be linked with real InSAR observations. Depending on site conditions such as deformation rate, land cover and data availability, this approach can be combined with multi-temporal methods such as SBAS-InSAR, DInSAR or PS-InSAR to improve temporal sampling and reduce noise and decorrelation effects. These developments support the use of satellite data in subsidence monitoring for the Mongolian mining sector.

The examples above highlight how satellite-based deformation measurements can be used in practice. Applying the method to real InSAR data involves several additional steps. The next section outlines a possible workflow for adapting the synthetic results of this thesis to a real site.

5.10 Application to Real InSAR Data: Conceptual Workflow

This thesis is based on synthetic experiments, but the same modeling and inversion steps can be adapted to real InSAR datasets with moderate adjustments. A practical application to a real site would follow the steps below:

1. Preprocess ascending and descending Sentinel-1 images.

LOS deformation maps would be generated using a time series technique such as Persistent Scatterer Interferometry (PSI) or SBAS. Atmospheric filtering, coherence masking, and phase-unwrapping corrections would be applied to produce stable LOS time series.

2. Align LOS rasters and define the analysis domain.

The ASC and DES rasters would be regridded to a common coordinate system and spatial resolution. Low-coherence areas would be removed. The modeling domain would be centered on the suspected subsidence region.

3. Set physical priors and parameter bounds.

Approximate values for depth H, expected influence angle β, and realistic ranges for μ and λ would be defined using geological information, mining geometry, cavern depth, or previous monitoring studies. These constraints help stabilize inversion on real, noisy data.

4. Forward modeling and LOS projection.

The analytical influence-function model would be evaluated using candidate parameter sets to generate vertical and horizontal displacement fields. These

fields would then be projected into the actual ASC and DES geometries of the processed Sentinel-1 datasets.

5. Parameter inversion and residual diagnostics.

Weighted nonlinear least squares would be applied to the stacked LOS observations. Residual maps, histograms, Q–Q plots, and per-orbit RMSE would be inspected to assess the noise model and identify atmospheric correlation or model mismatch.

6. Probabilistic or sequential estimation for time series.

If multiple epochs are available, Bayesian sampling or an Extended Kalman Filter could be used to update μ and λ over time. These approaches help separate noise from genuine changes in deformation dynamics.

7. Validation with external information.

Estimated parameters would be compared against independent datasets such as GNSS, leveling profiles, excavation depth, or known mining geometries. Structured residuals would be interpreted as indicators of asymmetry, heterogeneous geology, or deviations from the Gaussian model.

This conceptual workflow outlines how the synthetic framework developed in this thesis could be translated into a real-data application. A full demonstration is left for future work, but the steps show a clear path toward operational subsidence monitoring using combined ASC+DES InSAR observations.

6 Conclusion

This thesis examined how accurately three key subsidence parameters (the influence angle β, the convergence rate μ and the horizontal–tilt factor λ) can be obtained from synthetic InSAR line-of-sight (LOS) data under Sentinel-1-like viewing geometry and millimeter-level noise. Using a Gaussian influence function, explicit LOS projection and a series of controlled numerical tests, the study evaluated the quality of parameter estimation with weighted nonlinear least squares, Monte Carlo sampling, Bayesian methods and sequential updating. The results show how satellite geometry, noise conditions and the analytical deformation model affect the estimation of these parameters.

Answers to the Research Questions

RQ1. Recoverability of β, μ, and λ

When ascending and descending LOS data are combined, all three parameters can be estimated with high precision. For σ_{LOS} values of 1 to 2 mm, estimation errors remain below one percent, and the distribution of residuals matches the imposed noise. Monte Carlo experiments confirm narrow spreads for all parameters. These results indicate that β, μ and λ are clearly identifiable under the tested conditions.

RQ2. Effect of satellite viewing geometry

Viewing geometry strongly affects the estimation results. Single-track inversions (either ascending or descending only) do not introduce bias, but they lead to larger spreads and stronger coupling between parameters, particularly between β and λ. Using both viewing geometries together removes this ambiguity and improves estimation quality for all parameters, especially for λ, which reflects the horizontal response.

RQ3. Sensitivity to LOS noise

Parameter estimates remain essentially unbiased across the tested noise levels, but uncertainty increases in proportion to LOS noise. Doubling σ_{LOS} from 1 mm to 2 mm roughly doubles the parameter standard deviations. β is the least affected because it primarily controls trough width, while μ and λ show broader spreads due to their smaller influence on the LOS signal. Even at 2 mm noise, combined-geometry inversions remain stable and unbiased.

RQ4. Value of Bayesian and sequential estimation

Bayesian sampling provides full posterior distributions and credible intervals that agree with the Monte Carlo results. It also shows relationships between parameters, such as the small negative trend between β and μ. The sequential estimation test using an Extended Kalman Filter shows how estimates can be updated over multiple epochs. This is particularly useful for μ and λ, which respond to time-dependent changes in the subsidence model.

Future Work

Further development could focus on conditions that resemble real InSAR observations more closely. Possible directions include:

(i) adding spatially correlated atmospheric effects, coherence loss and possible unwrapping errors to the synthetic observations;
(ii) testing how the inversion behaves when the true deformation shape departs from the Gaussian form, for example by generating LOS data from asymmetric or geology-dependent models;
(iii) applying the method to a small real-world case and comparing the results with GNSS or leveling measurements, following the conceptual workflow outlined in Section 5.10;
(iv) estimating parameters by combining LOS data with external information; and
(v) integrating advanced InSAR time series techniques such as DInSAR, PS-InSAR and SBAS-InSAR, which would support the use of Sentinel-1

observations and improve the handling of temporal and atmospheric variation.

These steps would help move the numerical experiments presented in this thesis toward applications based on real InSAR data.

7 Bibliography

1. Avchar, A., Pal, S. K., Tripathi, A. K., & Kumar, G. (2024). Subsidence analysis for old abandoned board and pillar coal mines using ANSYS and Monte Carlo simulation. *Journal of Mining Science, 60*(3), 387–396. https://doi.org/10.1134/S1062739124030049

2. Babaryka, A., & Benndorf, J. (2025). New subsidence prediction method incorporating asymmetry and shape flexibility: A study case of salt caverns in North Germany. *Rock Mechanics and Rock Engineering, 58*, 8737–8751. https://doi.org/10.1007/s00603-025-04444-5

3. Bell, F. G., Stacey, T. R., & Genske, D. D. (2000). Mining subsidence and its effect on the environment: Some differing examples. *Environmental Geology, 40*(1–2), 135–152. https://doi.org/10.1007/s002540000140

4. Bérest, P., & Brouard, B. (2003). Safety of salt caverns used for underground storage: Blow out; mechanical instability; seepage; cavern abandonment. *Oil & Gas Science and Technology, 58*(3), 361–384. https://doi.org/10.2516/ogst:2003023

5. Brouard, B., Bérest, P., De Greef, V., Béraud, J. F., Lheur, C., & Hertz, E. (2013). Creep closure rate of a shallow salt cavern at Gellenoncourt, France. *International Journal of Rock Mechanics and Mining Sciences, 62*, 42–50. https://doi.org/10.1016/j.ijrmms.2012.12.030

6. Bürgmann, R., Rosen, P. A., & Fielding, E. J. (2000). Synthetic aperture radar interferometry to measure Earth's surface topography and its deformation. *Annual Review of Earth and Planetary Sciences, 28*, 169–209. https://doi.org/10.1146/annurev.earth.28.1.169

7. Burke, A., & Minsley, B. J. (2014). A trans-dimensional Bayesian Markov chain Monte Carlo algorithm for model assessment using

frequency-domain electromagnetic data. *Geophysical Journal International, 199*(3), 1666–1682. https://doi.org/10.1093/gji/ggu356

8. Chaussard, E., Amelung, F., Abidin, H., & Hong, S.-H. (2013). Sinking cities in Indonesia: ALOS PALSAR detects rapid subsidence due to groundwater and gas extraction. *Remote Sensing of Environment, 128*, 150–161. https://doi.org/10.1016/j.rse.2012.10.015

9. Colesanti, C., Ferretti, A., Novali, F., Prati, C., & Rocca, F. (2003). SAR monitoring of progressive and seasonal ground deformation using the permanent scatterers technique. *IEEE Transactions on Geoscience and Remote Sensing, 41*(7), 1685–1701. https://doi.org/10.1109/TGRS.2003.813278

10. Crosetto, M., Monserrat, O., Cuevas-González, M., Devanthéry, N., & Crippa, B. (2016). Persistent scatterer interferometry: A review. *ISPRS Journal of Photogrammetry and Remote Sensing, 115*, 78–89. https://doi.org/10.1016/j.isprsjprs.2015.10.011

11. Cyran. (2023). Insight into a shape of salt storage caverns. *Archives of Mining Sciences*. https://doi.org/10.24425/ams.2020.133198

12. Dong, L., Wang, C., Tang, Y., Tang, F., Zhang, H., Wang, J., & Duan, W. (2021). Time-series InSAR three-dimensional displacement inversion model of coal mining areas based on symmetrical features of mining subsidence. *Remote Sensing, 13*(11), 2143. https://doi.org/10.3390/rs13112143

13. Durup, J. G. (1994). Long-term subsidence from salt mining. In *Proceedings of the 6th International Symposium on Salt* (Vol. 2, pp. 1093–1100).

14. Energy.nl. (2021, December 16). Large-scale underground storage in salt caverns (Factsheet). https://energy.nl/

15. European Space Agency. (2013). Sentinel-1 user handbook. European Space Agency (ESA). https://sentinels.copernicus.eu/

16. European Space Agency. (2016). Sentinel-1 product definition (Issue 2/7). European Space Agency (ESA). https://sentinels.copernicus.eu/

17. Fan, H., Gu, W., Qin, Y., Xue, J., & Chen, B. (2014). A model for extracting large deformation mining subsidence using D-InSAR technique and probability integral method. *Transactions of Nonferrous Metals Society of China, 24*(4), 1242–1247. https://doi.org/10.1016/S1003-6326(14)63185-X

18. Fan, H., Zhang, D., Zhang, D., et al. (2021). Prediction of mining-induced surface subsidence by an improved probability integral method. *International Journal of Rock Mechanics and Mining Sciences, 144*, 104799. https://doi.org/10.1016/j.ijrmms.2021.104799

19. Ferretti, A., Prati, C., & Rocca, F. (2001). Permanent scatterers in SAR interferometry. *IEEE Transactions on Geoscience and Remote Sensing, 39*(1), 8–20. https://doi.org/10.1109/36.898661

20. Fuhrmann, T., & Garthwaite, M. C. (2019). Resolving three-dimensional surface motion with InSAR: Constraints from multi-geometry data fusion. *Remote Sensing, 11*(3), 241. https://doi.org/10.3390/rs11030241

21. Galloway, D. L., & Burbey, T. J. (2011). Review: Regional land subsidence accompanying groundwater extraction. *Hydrogeology Journal, 19*(8), 1459–1486. https://doi.org/10.1007/s10040-011-0775-5

22. Galloway, D. L., Jones, D. R., & Ingebritsen, S. E. (1999). *Land subsidence in the United States* (USGS Circular 1182).

23. Gelman, A., Carlin, J. B., Stern, H. S., & Rubin, D. B. (2004). *Bayesian data analysis* (2nd ed.). Chapman & Hall/CRC.

24. Gelman, A., Carlin, J. B., Stern, H. S., Dunson, D. B., Vehtari, A., & Rubin, D. B. (2013). *Bayesian data analysis* (3rd ed.). Chapman & Hall/CRC. https://doi.org/10.1201/b16018

25. Graves, A., Camacho, A. G., Fernández, J., García, A., & Romero, R. (2023). Bayesian MCMC inversion of surface deformation using InSAR. *Scientific Reports, 13*(1), 14692.

26. Graves, E. J., Rinehart, A., Grapenthin, R., Angarita, M. F., & Grigg, J. (2023). InSAR-observed surface deformation in New Mexico's Permian Basin shows threats and opportunities presented by leaky injection wells. *Scientific Reports, 13*(1), 17308. https://doi.org/10.1038/s41598-023-42696-9

27. Guzy, A., & Witkowski, W. T. (2021). Land subsidence estimation for aquifer drainage induced by underground mining. *Energies, 14*(15), 4658. https://doi.org/10.3390/en14154658

28. Hanssen, R. F. (2001). Radar interferometry: Data interpretation and error analysis. Springer. https://doi.org/10.1007/0-306-47633-9

29. Harati, S., & Rezaei Gomari, S. (2025). Designing geometrically stable salt caverns for underground hydrogen storage: A case study from northeast England. *Energy & Fuels*. https://doi.org/10.1021/acs.energyfuels.5c02957

30. Herrera, G., et al. (2021). Mapping and monitoring subsidence in the Madrid metropolitan area (Spain) with Sentinel-1 SAR interferometry. *Remote Sensing, 13*(1), 142. https://doi.org/10.3390/rs13010142

31. Hooper, A., Zebker, H., Segall, P., & Kampes, B. (2004). A new method for measuring deformation on volcanoes and other natural terrains using InSAR persistent scatterers. *Geophysical Research Letters, 31*(23), 2004GL021737. https://doi.org/10.1029/2004GL021737

32. Hou, Z., Yang, K., Li, Y., Gao, W., Wang, S., Ding, X., & Li, Y. (2022). Dynamic prediction model of mining subsidence combined with D-InSAR technical parameter inversion. *Environmental Earth Sciences, 81*, 307. https://doi.org/10.1007/s12665-022-10423-8

33. Jiang, Y., Misa, R., Tajduś, K., Sroka, A., & Jiang, Y. (2020). A new prediction model of surface subsidence with Cauchy distribution in the coal mine of thick topsoil condition. Archives of Mining Sciences, 65(1), 147–158. https://doi.org/10.24425/ams.2020.132712

34. Kalman, R. E. (1960). A new approach to linear filtering and prediction problems. *Journal of Basic Engineering, 82*(1), 35–45. https://doi.org/10.1115/1.3662552

35. Kaplan, G., Fine, L., Lukyanov, V., Manivasagam, V. S., Tanny, J., & Rozenstein, O. (2021). Normalizing the local incidence angle in Sentinel-1 imagery to improve leaf area index, vegetation height, and crop coefficient estimations. *Land, 10*(7), 680. https://doi.org/10.3390/land10070680

36. Karmis, M., Agioutantis, Z., & Jarosz, A. (1990). Recent developments in the application of the influence function method for ground movement predictions in the U.S. *Mining Science and Technology, 10*, 233–245. https://doi.org/10.1016/0167-9031(90)90439-Y

37. Ketelaar, V. B. H. (2009). *Satellite radar interferometry: Subsidence monitoring techniques*. Springer.

38. Koch, K.-R. (1999). *Parameter estimation and hypothesis testing in linear models*. Springer. https://doi.org/10.1007/978-3-662-03976-2

39. Kratzsch, H. (1983). *Mining subsidence engineering* (R. F. S. Fleming, Trans.). Springer-Verlag.

40. Kusche, J., & Klees, R. (2002). Regularization of gravity field estimation from satellite gravity gradients. *Journal of Geodesy, 76*(6–7), 359–368. https://doi.org/10.1007/s00190-002-0257-6

41. Li, P., Yang, T., Wang, Y., & Liu, Y. (2020). Study on the prediction of mining-induced surface subsidence using numerical modeling. *Journal of Geotechnical and Geoenvironmental Engineering, 146*(7), 04020058. https://doi.org/10.1061/(ASCE)GT.1943-5606.0002275

42. Ling, Q., Qu, W., Zhang, Q., Kong, L., Zhang, J., & Zhu, L. (2020). Improved Kalman filter method considering multiple factors and its application in landslide prediction. *Frontiers of Earth Science, 14*(3), 625–636. https://doi.org/10.1007/s11707-019-0796-2

43. Massonnet, D., & Feigl, K. L. (1998). Radar interferometry and its application to changes in the Earth's surface. *Reviews of Geophysics, 36*(4), 441–500. https://doi.org/10.1029/97RG03139

44. Peng, S. S. (2019). *Longwall mining* (3rd ed.). CRC Press. https://doi.org/10.1201/9780429260049

45. Saadat, M., Khishvand, M., Seccombe, A., & Campbell, R. (2025). A comprehensive Python tool for predicting mining-induced subsidence. In *ROC2025* (conference paper).

46. Samieie-Esfahany, S., Hanssen, R. F., van Thienen-Visser, K., & Muntendam-Bos, A. (2009). On the effect of horizontal deformation on InSAR subsidence estimates. In *Proceedings of the Fringe 2009 Workshop* (Frascati, Italy, 30 November–4 December 2009). ESA Publications.

47. Samsonov, S. V., & Tiampo, K. F. (2006). Analytical optimization of InSAR and GPS dataset combinations for derivation of three-dimensional surface

motion. *IEEE Transactions on Geoscience and Remote Sensing, 44*(1), 132–142. https://doi.org/10.1109/TGRS.2005.860950

48. Satbergenova, A., Talgarbayeva, D., Vilayev, A., Urazaliyev, A., Yelisseyeva, A., Kaldybayev, A., & Gavruk, S. (2025). InSAR-based assessment of land subsidence induced by coal mining in Karaganda, Kazakhstan. Geomatics, 5(4), 55. https://doi.org/10.3390/geomatics5040055

49. Sidki-Rius, N., Bascompta, M., Sanmiquel, L., & Yubero, M. T. (2024). Definition of characteristic subsidence parameters: A case study in the Catalan potassium basin. *Environmental Earth Sciences, 83*(19), 566. https://doi.org/10.1007/s12665-024-11849-y

50. Singh, B., & Singh, R. D. (1999). *Rock mechanics in mining practice*. Oxford & IBH Publishing.

51. Sroka, A., Misa, R., Tajduś, K., Klaus, M., Meyer, S., & Feldhaus, B. (2017). Forecast of rock mass and ground surface movements caused by the convergence of salt caverns for storage of liquid and gaseous energy carriers.

52. Tajduś, K. (2015). Numerical modeling of mining-induced horizontal displacement. In SGEM 2015 International Multidisciplinary Scientific GeoConference: Proceedings (Conference paper).

53. Tajduś, K., Misa, R., & Sroka, A. (2018). Analysis of the surface horizontal displacement changes due to longwall panel advance. *International Journal of Rock Mechanics and Mining Sciences, 104*, 119–125. https://doi.org/10.1016/j.ijrmms.2018.02.005

54. Tajduś, K., Sroka, A., & Misa, R. (2021). Analysis of mining-induced horizontal displacement distribution caused by mining exploitation. *Minerals, 11*(11), 1187. https://doi.org/10.3390/min11111187

55. Tandanand, S., & Powell, L. R. (1991). Determining horizontal displacement and strains due to subsidence (Report of Investigations 9358). U.S. Bureau of Mines.

56. Wang, L., Deng, K., & Zheng, M. (2020). Research on ground deformation monitoring method in mining areas using the probability integral model fusion D-InSAR, sub-band InSAR and offset-tracking. *International Journal of Applied Earth Observation and Geoinformation, 85*, 101981. https://doi.org/10.1016/j.jag.2019.101981

57. Wang, L., Li, N., Zhang, X., Wei, T., Chen, Y., & Zha, J. (2018). Full parameters inversion model for mining subsidence prediction using simulated annealing based on single line-of-sight D-InSAR. *Environmental Earth Sciences, 77*(5), 161. https://doi.org/10.1007/s12665-018-7355-0

58. Wang, R., et al. (2018). InSAR-based model parameter estimation of probability integral method for predicting mining-induced horizontal and vertical displacements. *Remote Sensing, 10*(8), 1271. https://doi.org/10.3390/rs10081271

59. Whittaker, B. N., & Pasamehmetoğlu, A. G. (1981). Ground tilt in relation to subsidence in longwall mining. *International Journal of Rock Mechanics and Mining Sciences & Geomechanics Abstracts, 18*(4), 321–329.

60. Whittaker, B. N., & Reddish, D. J. (1989). *Subsidence: Occurrence, prediction and control*. Elsevier.

61. Witkowski, W., Łukosz, M., Guzy, A., & Hejmanowski, R. (2021). Estimation of mining-induced horizontal strain tensor of land surface applying InSAR. *Minerals, 11*(7), 788. https://doi.org/10.3390/min11070788

62. Xie, Y., Bagan, H., Tan, L., Te, T., Damdinsuren, A., & Wang, Q. (2024). Time-series analysis of mining-induced subsidence in the arid region of

Mongolia based on SBAS-InSAR. *Remote Sensing, 16*(12), 2166. https://doi.org/10.3390/rs16122166

63. Xu, G. (Ed.). (2010). *Sciences of geodesy – I: Advances and future directions*. Springer. https://doi.org/10.1007/978-3-642-11741-1

64. Yang, Z., Li, Z., Zhu, J., Hu, J., Wang, Y., & Chen, G. (2016). InSAR-based model parameter estimation of probability integral method and its application for predicting mining-induced horizontal and vertical displacements. *IEEE Transactions on Geoscience and Remote Sensing, 54*(8), 4818–4832. https://doi.org/10.1109/TGRS.2016.2551779

65. Yang, Z., Li, Z., Zhu, J., Yi, H., Hu, J., & Feng, G. (2017). Deriving dynamic subsidence of coal mining areas using InSAR and logistic model. *Remote Sensing, 9*(2), 125. https://doi.org/10.3390/rs9020125

66. Yang, Z., Xu, B., Li, Z., Wu, L., & Zhu, J. (2022). Prediction of mining-induced kinematic 3-D displacements from InSAR using a Weibull model and a Kalman filter. *IEEE Transactions on Geoscience and Remote Sensing, 60*, 4500912. https://doi.org/10.1109/TGRS.2021.3055854

67. Zebker, H. A., & Villasenor, J. (1992). Decorrelation in interferometric radar echoes. *IEEE Transactions on Geoscience and Remote Sensing, 30*(5), 950–959. https://doi.org/10.1109/36.175330

68. Zhang, B., Cui, X., Zhao, Y., & Li, C. (2021). Prediction model and algorithm for dynamic subsidence of inclined main section. *Journal of China Coal Society, 46*(6), 1864–1873. https://doi.org/10.13225/j.cnki.jccs.2019.1814

69. Zhang, G., Xu, Z., Chen, Z., Wang, S., Cui, H., & Zheng, Y. (2022). Predictable condition analysis and prediction method of SBAS-InSAR coal mining subsidence. *IEEE Transactions on Geoscience and Remote Sensing, 60*, 1–14. https://doi.org/10.1109/TGRS.2022.3195269

Appendix A – Dual orbit InSAR synthetic test and analytic Jacobian (ASC+ DES)

A.1 Summary of parameter recovery (single-epoch synthetic tests)

Tables A1–A2 report the mean ±1σ estimates for the look-plane angle β, the convergence rate μ (yr^{-1}), and the dimensionless shape/coupling parameter λ, for two LOS noise levels (σ_LOS = 1 and 2 mm) and three true λ values (0.3, 0.5, 1.0). In both ascending (ASC) and descending (DES) geometries, β is recovered at ≈45° and μ at 0.010 yr^{-1} with uncertainties that scale sensibly with the imposed LOS noise; λ is unbiased within about ±0.01.

Table A 1. ASC geometry: recovery vs. noise and λ (mean ±1σ).

	λ true	σ_LOS [mm]	β [deg]	μ [yr^{-1}]	λ [-]
ASC	0.3	1	44.995 ± 0.124	0.01000 ± 0.00007	0.300 ± 0.005
	0.3	2	45.018 ± 0.246	0.01001 ± 0.00015	0.301 ± 0.010
	0.5	1	45.006 ± 0.111	0.00999 ± 0.00007	0.500 ± 0.005
	0.5	2	45.021 ± 0.252	0.00999 ± 0.00013	0.500 ± 0.010
	1	1	45.001 ± 0.066	0.01000 ± 0.00005	1.000 ± 0.007
	1	2	45.008 ± 0.151	0.01000 ± 0.00011	1.000 ± 0.013

Table A 2. DES geometry: recovery vs. noise and λ (mean ±1σ)

	λ true	σ_LOS [mm]	β [deg]	μ [yr^{-1}]	λ [-]
DES	0.3	1	44.990 ± 0.130	0.01002 ± 0.00007	0.299 ± 0.004
	0.3	2	45.004 ± 0.256	0.01000 ± 0.00014	0.301 ± 0.009
	0.5	1	45.011 ± 0.119	0.01000 ± 0.00006	0.500 ± 0.005
	0.5	2	45.017 ± 0.225	0.00997 ± 0.00013	0.502 ± 0.009
	1	1	45.008 ± 0.063	0.01000 ± 0.00006	0.999 ± 0.007
	1	2	44.965 ± 0.125	0.01001 ± 0.00009	1.001 ± 0.013

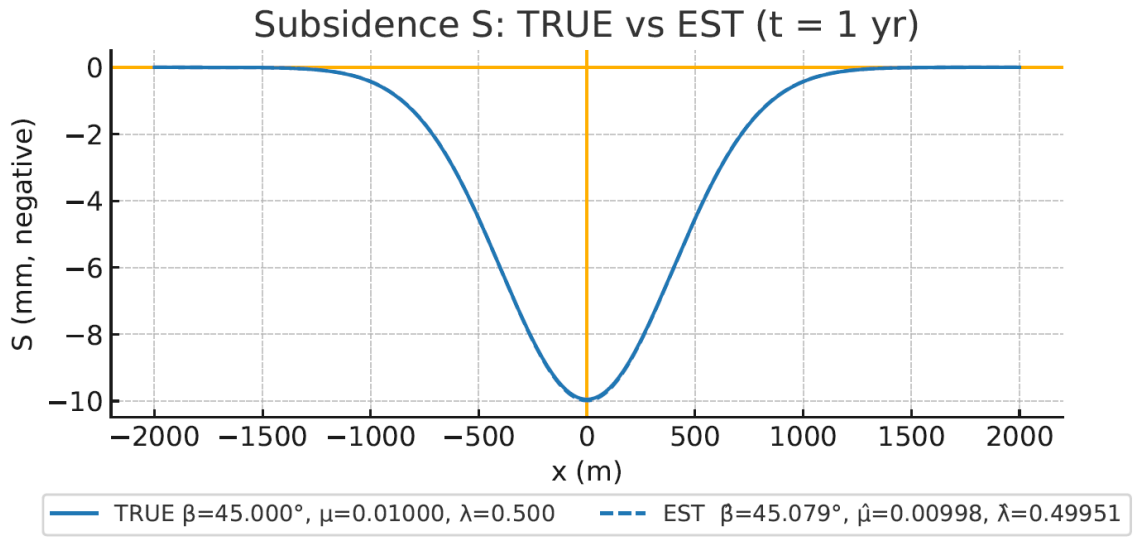

Figure A 1. Subsidence S: Forward (True) vs. Estimated (EST) overlay (−S in mm)

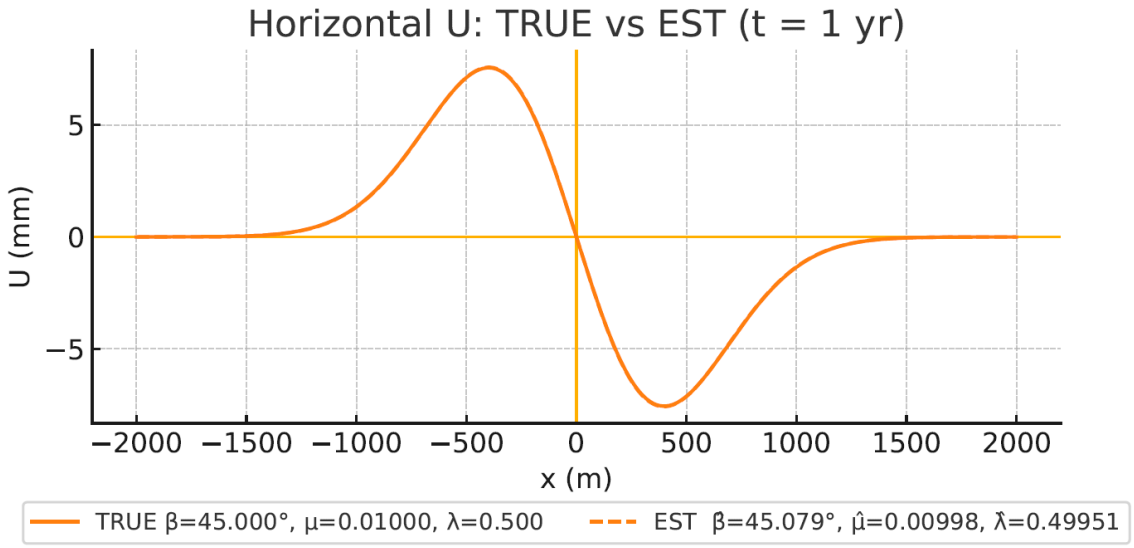

Figure A 2. Horizontal U: Forward (True) vs. Estimated (EST) overlay (mm)

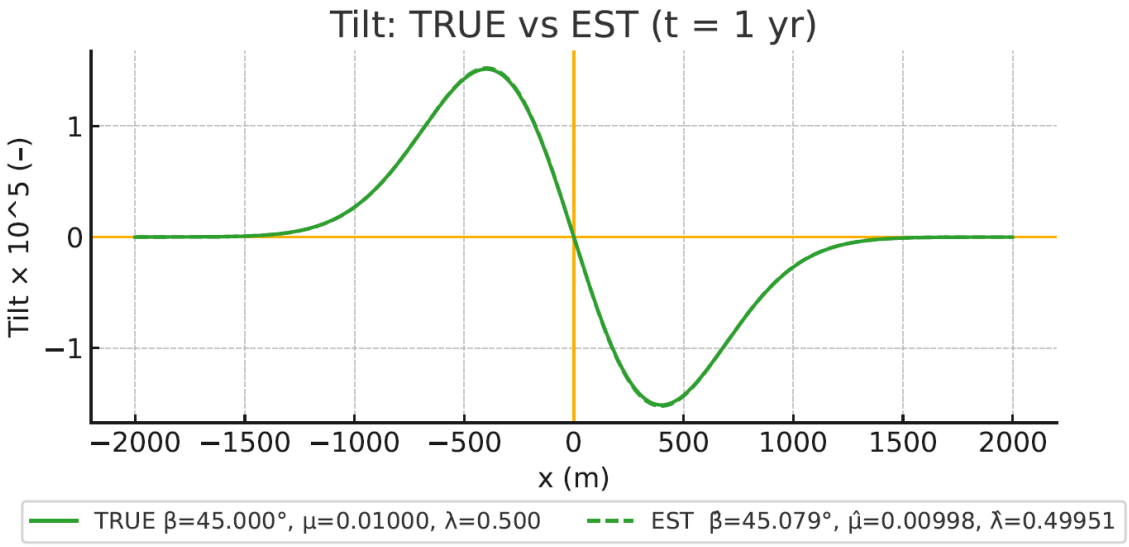

Figure A 3. Tilt: Forward (True) vs. Estimated (EST) overlay (×10⁵)

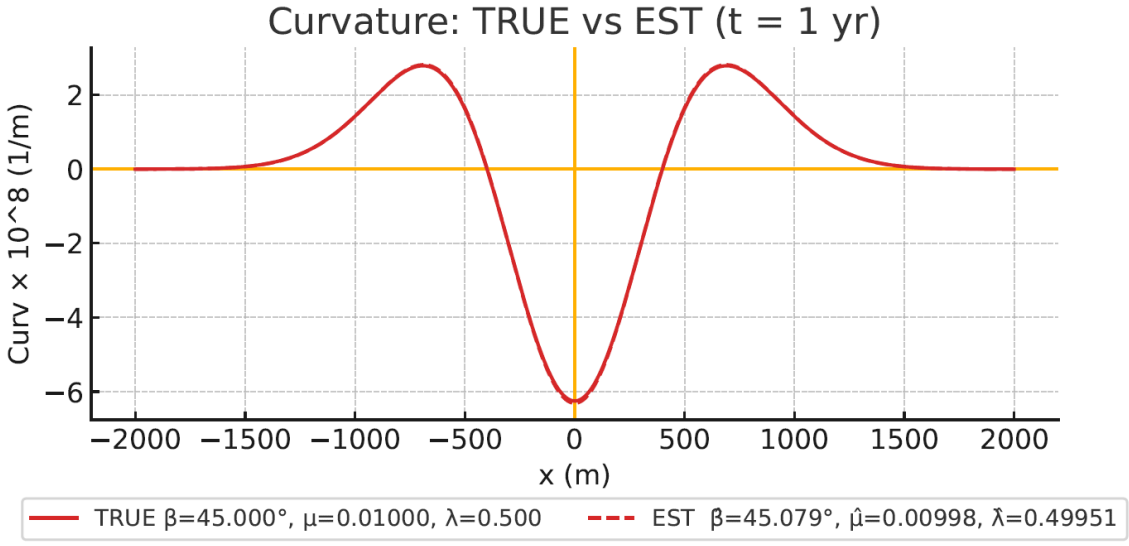

Figure A 4. Forward (True) vs. Estimated (EST) overlay (×10⁸)

A2. Dual-orbit NLSQ and temporal behavior

Epoch scaling & model consistency. With baseline geometry (R = 1000 m), the trough depth in Epoch 2 is ≈1.98× Epoch 1 - exactly what the exponential convergence model with μ = 0.01 yr^{-1} predicts. The maximum LOS gradient and the largest ASC–DES separation occur near $r \approx R/\sqrt{2\pi}$, i.e., ≈399 m for R=1000 m.

Fit quality & parameter sensitivity. A joint inversion of ASC+DES fits both epochs with ~1 mm RMSE; adding a second epoch sharpens sensitivity to μ while leaving β and λ stable.

Sum & difference channels. The sum channel isolates the vertical subsidence S, while the difference channel isolates the horizontal component U aligned with the look direction.

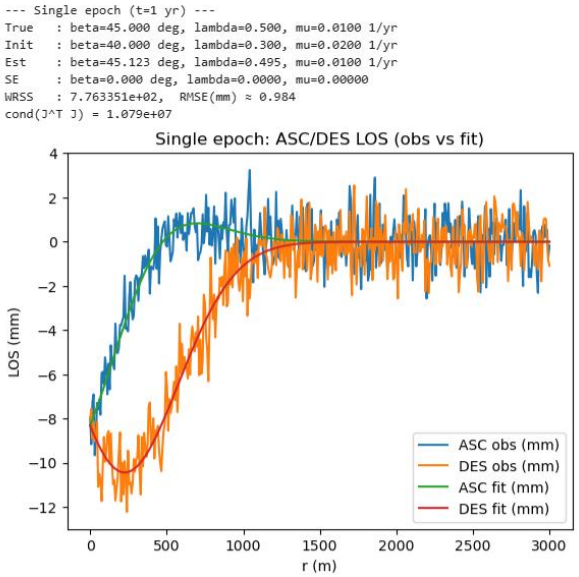

Figure A 5. Single-epoch ASC/DES LOS (observations vs. fit); shows initial fit quality and orbit-dependent shoulder behavior.

```
--- Two epochs (t=1,2 yr) ---
True   : beta=45.000 deg, lambda=0.500, mu=0.0100 1/yr
Init   : beta=40.000 deg, lambda=0.300, mu=0.0200 1/yr
Est    : beta=44.980 deg, lambda=0.494, mu=0.0100 1/yr
SE     : beta=0.000 deg, lambda=0.0000, mu=0.00000
WRSS   : 1.650122e+03,  RMSE(mm) ≈ 1.014
cond(J^T J) = 1.060e+07
```

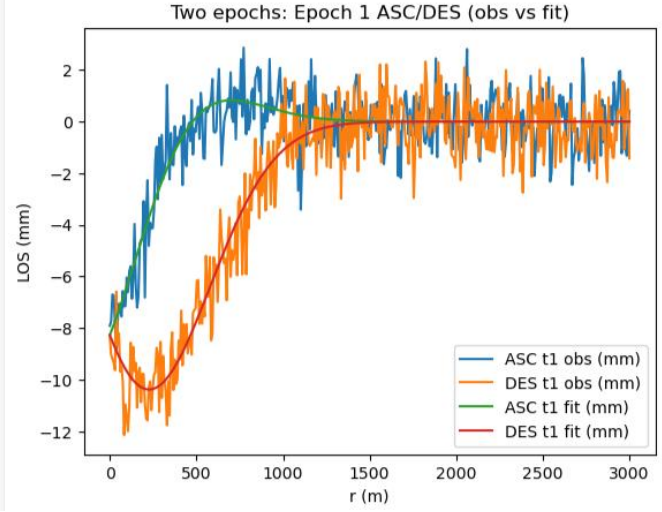

Figure A 6. Two-epoch, Epoch-1 ASC/DES (obs vs. fit); establishes baseline trough.

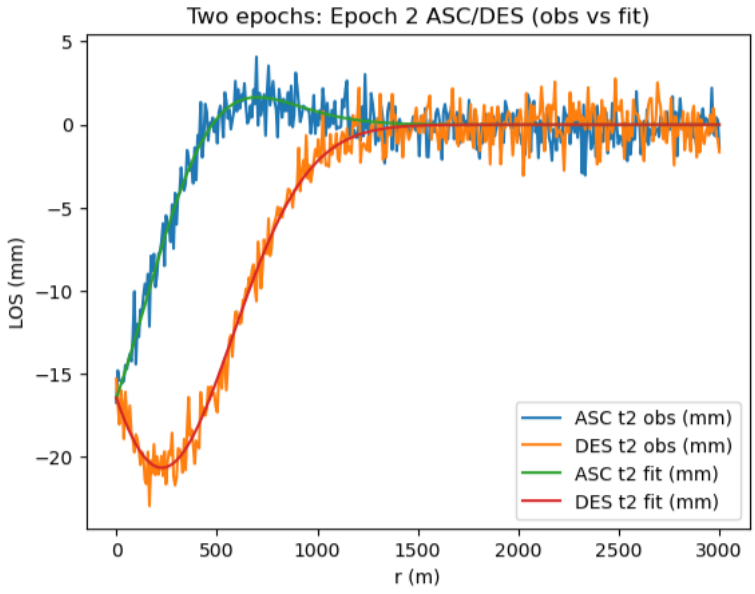

Figure A 7. Two-epoch, Epoch-2 ASC/DES (obs vs. fit); trough depth ≈1.98× Epoch-1 as predicted by μ=0.01 yr⁻¹.

A3. Effects of λ on horizontal and LOS signals

Horizontal displacement u_{east}: Increasing λ amplifies the radial/horizontal response and shapes the LOS shoulder.

ASC/DES profiles: LOS profiles for ASC and DES respond smoothly to λ; the shoulder region shows the strongest ASC–DES divergence due to U.

β robustness to noise: Recovered β stays near 45° even as LOS noise increases, across λ ∈ {0.3, 0.5, 1.0}.

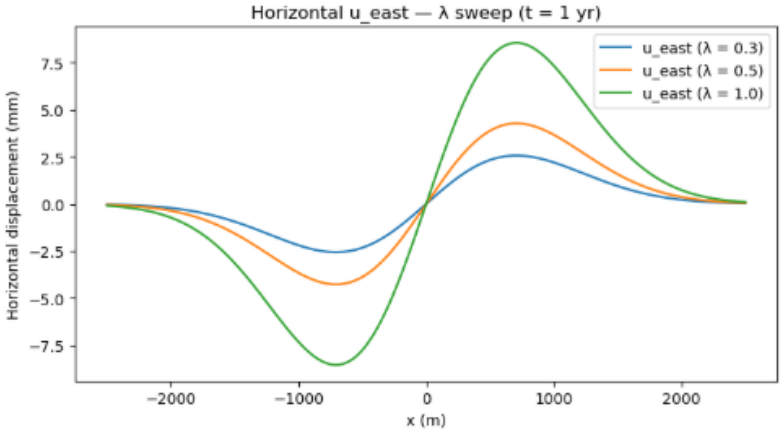

Figure A 8. λ-sweep of u_{east} and ASC LOS at t=1 yr; horizontal amplification with λ.

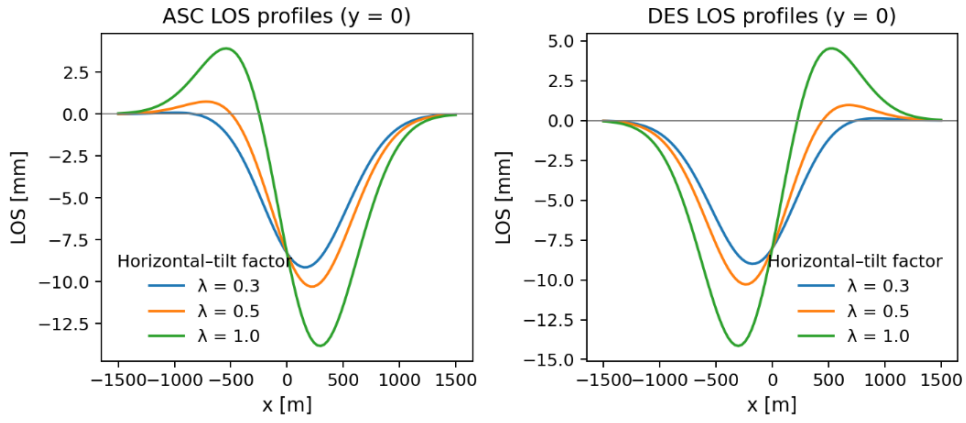

Figure A 9. DESC LOS λ-sweep and orbitwise profiles at y=0; symmetric sag at center, orbit split in shoulders.

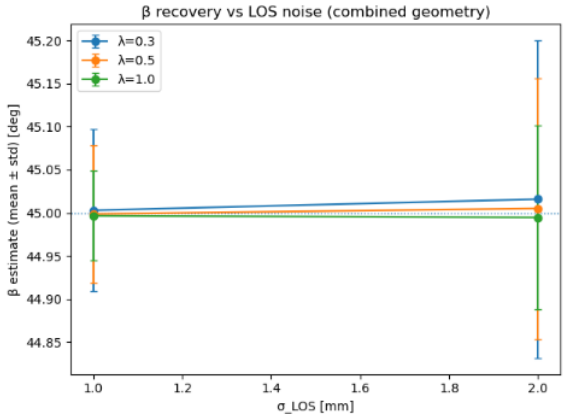

Figure A 10. recovery vs. LOS noise (combined geometry); stability of β across λ and noise.

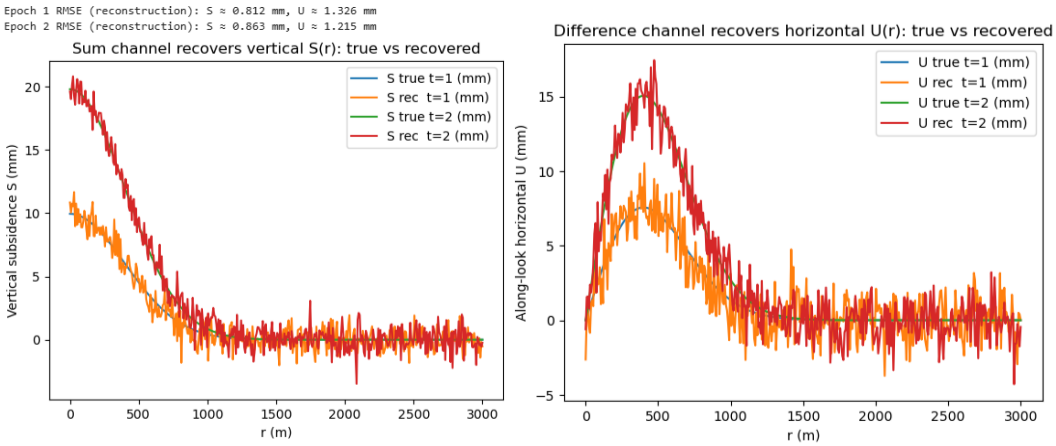

Figure A 11. Sum channel ≈ vertical S; difference channel ≈ horizontal U; *demonstrates the standard decomposition.*

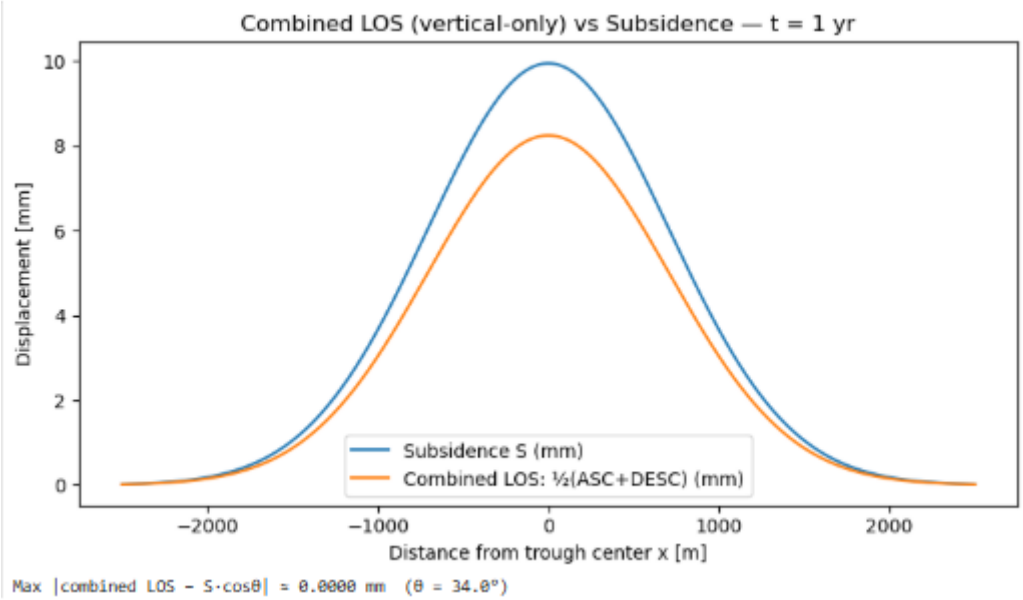

Figure A 12. Combined (ASC+DES) LOS vs vertical-only S; max difference ≈0.48 mm for θ≈34°

Appendix B – Code Structure and Reproducibility

All numerical experiments for this thesis were implemented in Python using the libraries NumPy, SciPy, pandas, matplotlib, and emcee. The code is organized into two files to separate the core reproducible workflow from extended diagnostics and supplementary experiments.

B.1 Main Workflow (01_main_model_and_inversion.py)

This file contains the complete modelling and inversion workflow used to produce the figures and tables in Chapters 3 and 4. It includes:

- generation of synthetic subsidence, tilt, and horizontal displacement,
- LOS projection for ascending and descending satellite geometry,
- weighted nonlinear least-squares estimation of (β, μ, λ),
- Monte-Carlo uncertainty analysis,
- Laplace approximation for posterior covariance,
- MCMC sampling for Bayesian inference,

- Extended Kalman Filtering (EKF) for sequential multi-epoch estimation,
- saving of all final thesis figures and tables.

Running this file reproduces all core results reported in the thesis.

B.2 Extended Experiments (02_extended_experiments.py)

This file contains additional analyses that support or expand the main results. These experiments are supplementary and not required to reproduce the primary findings, but they provide deeper insight into:

- residual histograms and Q–Q diagnostics,
- mode comparison (ASC-only, DES-only, combined),
- sensitivity sweeps for λ, incidence angles, and noise levels,
- additional Monte-Carlo sampling,
- extended visualizations used during development and validation.

The extended file complements the main workflow and documents further exploration of model behavior.

B.3 Reproducibility

All figures generated by the scripts are saved automatically into the folders:

- *chap3_figs/* and *chap4_figs/* — figure outputs
- *chap3_tables/* and *chap4_tables/* — CSV tables and numerical summaries

The Python implementation requires the following packages:

- NumPy
- pandas
- matplotlib
- SciPy

- emcee

These can be installed using standard package managers such as pip.

Both code files are included in the electronic submission to ensure full reproducibility of all results.